Journal of Sound and Vibration 644 (2026) 120066

Contents lists available at ScienceDirect

Journal of Sound and Vibration

journal homepage: www.elsevier.com/locate/jsvi

Force-scaling rated load correction method for stable quasi-zero-stiffness vibration isolation

Jia-Jia Lu [b], Tian-Yu Zhao [a], Fan-Chi Zeng [a], Wen-Hao Qi [a], Ge Yan [a], Li Cheng [b,*], Wen-Ming Zhang [a,*]

[a] State Key Laboratory of Mechanical System and Vibration, School of Mechanical Engineering, Shanghai Jiao Tong University, 800 Dongchuan Road, Shanghai, 200240, China

[b] Department of Mechanical Engineering, Hong Kong Polytechnic University, Hung Hom, Kowloon, 999077, Hong Kong

A R T I C L E I N F O

Keywords:
Quasi-zero-stiffness
Load mismatch
Rated load correction
Vibration isolation
Low-frequency vibration

A B S T R A C T

The ability of quasi-zero-stiffness (QZS) vibration isolators to deliver stable low-frequency vibration isolation is hindered by load mismatch. Herein, a force-scaling rated load correction method is proposed and investigated to enhance the stability of QZS vibration isolation. By scaling the force-displacement curve, the *in-situ*, continuous, and wide-range rated load correction is achieved to eliminate load mismatches while preserving a constant natural frequency. To validate the method, a rated load corrector (RLC) is developed by leveraging the positive correlation between electromagnetic force and input current, and integrated into a passive QZS isolator featuring ultra-low dynamic stiffness. Static and dynamic comparisons with the conventional rated load correction are conducted to reveal the underlying mechanism that enables stable low-frequency vibration isolation performance. Base excitation test results show that, without the force-scaling rated load correction, the performance of the passive QZS isolator, with a starting isolation frequency of 0.8 Hz, deteriorates markedly under a minor load mismatch of 10 g (0.31% of the rated load). In contrast, with the correction, load mismatches ranging from 0.31% to 25% of the rated load are effectively mitigated while maintaining comparable performance. These results demonstrate that the proposed method substantially improves the stability of passive QZS isolators for low-frequency vibration isolation.

1. Introduction

Harmful vibrations are common in various precision instruments and equipment, such as atomic force microscopes, precision machine tools, and orbital optical satellites, where they can unexpectedly degrade equipment performance [1–3], shorten device lifespan [4–6], or even lead to serious workplace accidents [7]. As an effective method for suppressing adverse vibrations, vibration isolation can block energy transmission from the vibration source to the sensitive object through elastic deflection, damping-induced energy dissipation, and inertial motion. According to linear vibration theory, achieving low-frequency vibration isolation is challenging due to the positive correlation between the resonant frequency and the starting isolation frequency [8,9]. While reducing the stiffness of a vibration isolator can effectively reduce its resonant frequency, it inevitably causes excessive static deflection, thereby

* Corresponding authors.
E-mail addresses: jiajiaturbo.lu@polyu.edu.hk (J.-J. Lu), zhaotianyu@sjtu.edu.cn (T.-Y. Zhao), fanchizeng@sjtu.edu.cn (F.-C. Zeng), qiwenhao@sjtu.edu.cn (W.-H. Qi), sjtuyange@sjtu.edu.cn (G. Yan), li.cheng@polyu.edu.hk (L. Cheng), wenmingz@sjtu.edu.cn (W.-M. Zhang).

https://doi.org/10.1016/j.jsv.2026.120066
Received 29 March 2026; Received in revised form 17 June 2026; Accepted 11 August 2026
Available online 11 August 2026

limiting the load-bearing capacity and compromising system stability.

Nomenclature	
QZS	quasi-zero-stiffness
RLC	rated load corrector
HSLDS	high static and low dynamic stiffness
CCBS	passive QZS isolator
QZS-RLC	passive QZS isolator incorporating the RLC
RKM	Runge-Kutta Method
RMS	root-mean-square
F_{pas}, F_{cor}, F_c	restoring forces of the passive QZS isolator, RLC, and QZS-RLC
q_n, p_n	polynomial fitting coefficients
N_p, N_q	polynomial order
x	displacement
α	scaling coefficient
F_{pe}, F_{ce}	rated loads of the passive QZS isolator and QZS-RLC
F_{re}	rated load of the RLC when α=1
k_{pas}, k_{cor}, k_c	stiffnesses of the passive QZS isolator, RLC, and QZS-RLC
k_{pe}, k_{ce}	minimum stiffnesses at the equilibrium position of the passive QZS isolator and QZS-RLC
F_{re}	stiffness at the equilibrium position of the RLC when α=1
$\boldsymbol{R}_c$, $\boldsymbol{R}_s$	position vectors of any point P_c on the coil wire loop and any point P_s on the solenoid wire loop
r_c, z_c	radius and z coordinate of the coil wire loop
r_s, z_s	radius and z coordinate of the solenoid wire loop
φ_s	angle between the projection of $\boldsymbol{R}_s$ on the xoy plane and the x-axis
φ_c	angle between the projection of $\boldsymbol{R}_c$ on the xoy plane and the x-axis
$\boldsymbol{i}, \boldsymbol{j}, \boldsymbol{k}$	basis vectors
$\boldsymbol{B}$	magnetic induction intensity at the point P_c
$I_c\mathrm{d}\boldsymbol{l}_c$, $I_s\mathrm{d}\boldsymbol{l}_s$	current elements of the coil wire loop and the solenoid wire loop
I_c, I_s	currents of the coil wire loop and the solenoid wire loop
μ_0	vacuum permeability
B_x, B_y, B_z	magnetic flux density in the x, y, and z directions
F_z	electromagnetic force along the z-axis
B_r	residual magnetic flux density of the permanent magnet
r_m, h_m, w_m	inner radius, width and height of the permanent magnet
N_m	the number of the wire loops of the permanent magnet
z_m	z coordinate of the bottom surface of the permanent magnet
r_c, w_c, h_c	inner radius, width, and height of the coil
i	type of the solenoid, where $i = 1$ and $i = 2$ represent the inner and outer solenoids
j	type of the coil, where $j = 1$ and $j = 2$ represent the negative-stiffness coil and the positive-stiffness coil
z_{cj}	z coordinate of the bottom surface of the coil
N_{wj}, N_{hj}	the number of wire loops in the radial direction and the axial direction
r_{mi}, z_{mi}	radius and z coordinate of the p_i-th wire loop of the inner solenoid or the outer solenoid
I_{cj}	current of the coil
k, k_{ij}	elliptic parameters
r_{sj}, z_{ti}	radius and z coordinate of each wire loop of the negative-stiffness and positive-stiffness coils
q_r, p_r, s_r, v_r, w_r	polynomial fitting coefficients
d_m	displacement when the permeant magnet is initially compressed
I_r	current ratio
F_p	restoring force (passive QZS isolator)
F_c	restoring force (QZS-RLC)
d_t	variation in the screw-in length of the coil holder
d_s	equilibrium position of the passive QZS
k_l	linear positive-stiffness
F_b	restoring force of the bistable negative-stiffness element
d_l	variation in compression of the linear positive-stiffness element
m_{pe}, m_{re}	rated loads of the passive QZS isolator and RLC
α	scaling coefficient
I_{c10}, I_{c20}	initial current configuration of the negative-stiffness and positive-stiffness coils
ζ	damping coefficient
m	lumped mass
c	damping
g	gravitational acceleration constant
z_b	base excitation
a_b, ω	excitation amplitude, angular frequency of the base excitation
z_r	relative displacement response of the mass
z	absolute displacement response of the mass
a_0, a_1, φ	amplitude, offset, and phase of the relative displacement response
t	time
$\bar{p}_i$	auxiliary variable
T_d	displacement transmissibility

The emergence of QZS vibration isolators addresses the aforementioned dilemma of linear vibration isolation. By introducing stiffness nonlinearity to linear vibration isolators, the QZS isolators possess a high static stiffness for bearing applied load and a low dynamic stiffness for lowering resonant frequency, thereby enabling a small starting isolation frequency without depriving of load-carrying capacity [10–13]. In recent decades, bistable nonlinearity has been widely employed in the design of QZS isolators. The negative stiffness structures inherently associated with bistable nonlinearity can counterbalance the linear springs of conventional linear isolators to obtain the high static and low dynamic stiffness (HSLDS) characteristic [14]. Typical structures that exhibit bistable nonlinearity include, but not limited to, oblique springs [15–17], link-spring mechanisms [18–21], buckled beams [22–25], cam-roller mechanisms [26–28], magnetic structures [29–32], X-shaped structures [33–36], bionic structures [37–40], and origami mechanisms [41–44]. In most cases, their bistable behavior originates from geometric or magnetic nonlinearity. By scaling down the QZS structures into unit cells and arranging them in a specific pattern, QZS metamaterials have been widely constructed with high compactness and flexible customization [45–47]. In contrast, Yan et al. [48,49] replaced linear positive stiffness with hardening positive stiffness to construct QZS isolators, referred to as a nonlinear compensation mechanism, which eliminates dependence on bistable nonlinearity for achieving the HSLDS characteristic. A variety of QZS isolators have been developed based on the nonlinear compensation mechanism, employing mutually repelling magnets [50–52] or membrane springs [53] as hardening elastic elements. However, the QZS characteristic is not a sufficient condition for effective low-frequency vibration isolation. Since the QZS behavior reflects a nonlinear stiffness characteristic in which displacement, force, and stiffness are intrinsically coupled, only when QZS isolators are loaded to the equilibrium position of low dynamic stiffness can they achieve a low resonant frequency and, consequently, effective low-frequency vibration isolation. Therefore, when the applied load deviates from the rated load, the inherent nonlinearity of the QZS isolator exhibits more complex dynamic behavior [54,55], resulting in a deterioration of its low-frequency vibration isolation performance. References [56–58] investigated the dynamic behavior of QZS isolators under load imperfection, and found that as the applied load gradually deviates from the rated value, the asymmetry of the system deepens, the starting isolation frequency increases, and the transmissibility curve sequentially shows the characteristics of pure hardening, softening followed by hardening, and pure softening. The dynamic behavior becomes highly complex, and the system stability weakens. Furthermore, the higher the desired isolation performance at low frequencies, the smaller the required dynamic stiffness, making the system more sensitive to load mismatch. Consequently, QZS isolators are struggling to robustly suppress ultra-low frequency vibrations under variable applied loads.

To prevent the degradation of low-frequency vibration isolation performance due to load mismatch, recent studies primarily focused on load compensation and rated load adjustment. The load compensation method employs an active actuator to generate a constant force that counteracts load mismatches without altering the rated load and stiffness characteristic of the passive QZS isolator. Qi et al. [59] proposed a local gravity control method to address the load-mismatch issue in isolators. Under closed-loop feedback control, the actuator is capable of producing a prescribed constant compensating force. Sun et al. [60] integrated an electromagnetic actuator into a passive QZS isolator. The improved particle swarm optimization algorithm was employed to optimize the Proportion-Integration-Differentiation controller, enabling the actuator to produce a constant force for compensating varying load mismatches. In contrast, rated load adjustment methods can generally be divided into three categories: modifying the compression of the linear spring, designing multiple QZS regions, and implementing active or semi-active approaches. For QZS isolators connecting bistable structures in parallel with linear springs, the load is primarily borne by the linear springs, allowing for rated load adjustment through spring compression adjustment [61–63]. Lan et al. [64] used bolts to adjust the compression of the linear spring. By rotating the bolts, the restoring force of the linear spring can be modified, thereby achieving rated load adjustment. Chang et al. [65] further developed a non-manual rated load adjustment mechanism based on a step motor, a screw, and a driving mechanism, which enables labor-saving adjustment of the rated load. Designing multiple QZS regions offers an alternative approach to mitigating the sensitivity of QZS isolators to variations in applied load. When the applied load changes, the operating position of the vibration isolator shifts from its initial equilibrium position into another low dynamic stiffness region, allowing for continuous maintenance of the QZS characteristic [66,67]. Ye et al. [68] proposed a QZS isolator capable of adapting to varying applied loads. Unlike the classic cam-roller mechanism, their design increases the number of cams, facilitating the roller to contact different cams as the applied load changes. This interaction generates negative stiffness at multiple locations, and thus several low-stiffness intervals on the force-displacement curve are successfully created. Meng et al. [69] designed a QZS isolator with three zero stiffness points using four inclined springs and two horizontal springs, enabling effective vibration isolation for multiple masses. Zhang et al. [70] combined a series of metamaterial cells with different QZS characteristics in series, enabling the customization of a force-displacement curve featuring multiple low-stiffness regions. Active and semi-active rated load adjustment is another option. For example, Jing et al. [71,72] developed a bioinspired dynamics-based adaptive tracking control method for suspension systems, which used a bionic QZS structure as the tracking reference. This method allows the suspension system to emulate the dynamic features of the QZS structure to effectively achieve adaptive vibration isolation under unknown applied loads. Vo and Le [73] developed a pneumatic vibration isolation platform that integrates pneumatic springs and cam-roller mechanism. A design procedure was proposed to ensure zero stiffness at the equilibrium position by adjusting the pneumatic stiffness. In our previous work [74], a load-adaptive electromagnetic QZS isolator was developed by connecting nonlinear electromagnetic negative- and positive-stiffness structures in parallel. Through active regulation of both nonlinear positive and negative stiffness, the QZS isolator can adapt to time-varying applied loads. Nevertheless, such a fully energy-driven QZS isolator demands considerable energy input to achieve a high-bearing capacity and would fail once the energy supply is interrupted.

According to the literature review, rated load adjustment can be achieved through a mechanical feed mechanism that alters the compression of the linear spring. However, the compression adjustment of the linear spring cannot alter the stiffness characteristics of the isolator, resulting in a variation of the natural frequency as the rated load changes. Meanwhile, the method of adjusting the rated load by constructing multiple low-stiffness intervals is inherently discrete and unsuitable for applications with continuously varying applied loads. In addition, active methods can achieve load adaptation through uninterrupted feedback control. However, once the active control fails, these methods lose their load regulation capability, which in turn degrades low-frequency vibration isolation performance, showing poor reliability. Existing semi-active QZS isolators mainly focus on preserving the QZS characteristic at the equilibrium position as applied loads varies, while the variation of the natural frequency under different loads is rarely considered. Moreover, semi-active QZS isolators generally require substantial energy input to achieve high load-bearing capacity. To abridge the current research gap, this paper proposes a force-scaling rated load correction method that enables *in-situ* and continuous adjustment of the rated load in QZS isolators while preserving the natural frequency and ensuring stable low-frequency vibration isolation performance. In contrast to conventional methods, which either depend on feedback control to achieve constant force output or are unable to maintain a stable natural frequency, the proposed method avoids the need for feedback control while still delivering quasi-constant force and maintaining constant natural frequency. Table 1 summarizes and compares various load compensation and load adjustment methods in terms of their adjustment principles, feedback control requirements, continuity of load variation, ability to preserve the natural frequency, energy input requirements, and isolation stability. With the aim of validating the proposed method, an RLC is developed, exploiting the proportional relationship between electromagnetic force and input current. The RLC is integrated with a passive QZS isolator to fulfill the rated load correction under time-varying applied loads. Electromagnetic force modeling and experimental testing of the RLC are conducted to demonstrate its force-scalable characteristics for the force-scaling rated load correction. Furthermore, theoretical comparison with the conventional rated load correction method and rated load correction experiments are performed to highlight and verify the advantages of the force-scaling rated load correction method in achieving stable low-frequency vibration isolation for passive QZS isolators.

The remainder of this paper is organized as follows. Section 2 elaborates on the force-scaling rated load correction method and the conceptual design of the RLC. Section 3 describes the implementation procedure of force-scaling rated load correction. In Sections 4 and 5, static and dynamic comparisons with the conventional rated load correction are conducted, respectively, to highlight the advantages of the proposed method. Section 6 demonstrates the effectiveness of the proposed force-scaling rated load correction method through rated load correction experiments. Finally, Section 7 concludes the paper.

2. Methodology and design

2.1. Force-scaling rated load correction method

As shown in Fig. 1(a), the QZS isolators feature a nonlinear force-displacement relationship. Initially, as displacement increases, the restoring force rises with a decreasing rate, demonstrating a softening behavior. After passing the inflection point E, the restoring force begins to rise at an increasing rate, indicating a hardening behavior. At the inflection point, the QZS isolators exhibit the HSLDS characteristic. As a result, when a QZS isolator is loaded to the inflection point, the starting isolation frequency is small, achieving excellent low-frequency vibration isolation performance. Traditionally, the inflection point is defined as the equilibrium position, and the corresponding applied load is defined as the rated load. However, due to stiffness nonlinearity, when the applied load mismatches the rated value, the load will deviate away from the equilibrium position of minimum stiffness to other points, such as points A and B, causing the disappearance of the QZS characteristic. As illustrated in Fig. 1(b), consequently, the starting isolation frequency increases, narrowing the vibration isolation bandwidth and degrading low-frequency vibration isolation performance. If an ultra-low starting isolation frequency is required, the stiffness at the equilibrium position should be very small, which makes the performance degradation due to load mismatch easier to occur. Therefore, it is a challenge for QZS isolators to realize stable low-frequency vibration isolation under variable applied loads. This inherent drawback of QZS isolators can be addressed via force-scaling rated load correction. Fig. 1(c) gives the force-displacement curves of a passive QZS isolator with an RLC. The RLC is designed with the QZS characteristic, and its force-displacement curve can be scaled to adjust its rated load without changing the equilibrium position. Using polynomial fitting, the force-displacement relationships of the passive QZS isolator, the RLC and the passive QZS isolator incorporating the RLC (QZS-RLC) can be expressed as

Table 1
Summary and comparison of various load compensation and load adjustment methods.

Methods	Principle	Feedback control	Load variation	Natural frequency	Energy input	Isolation stability
Active load Compensation [59,60]	Output constant force to compensate load variation	Necessary	Continuous	Changed	Low	Low
Linear spring adjustment [64,65]	Alter the spring compression to adjust the rated load	Unnecessary	Continuous	Changed	Unnecessary	Low
Multi QZS regions [68–70]	Construct multiple QZS regions for bearing various loads	Unnecessary	Discontinuous	Changed	Unnecessary	Low
Active rated load adjustment [71,72]	Emulate the response of the QZS system	Necessary	Continuous	Changed	Low	Low
Semi-active rated load adjustment [73]	Regulate both the positive and negative stiffnesses to preserve the QZS characteristic	Unnecessary	Continuous	Changed	High	Low
Force-scaling rated load correction (Our work)	Scale the restoring force of the corrector to correct the rated load	Unnecessary	Continuous	Unchanged	Low	High

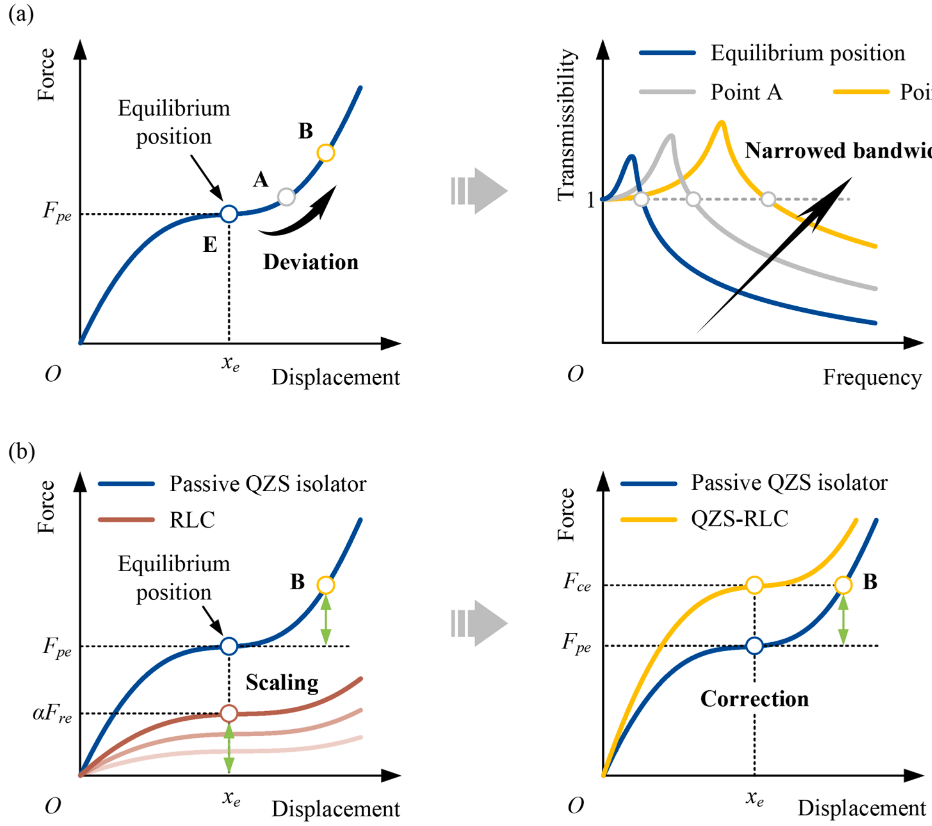

Fig. 1. Force-scaling rated load correction method: (a) performance degradation of the QZS isolators caused by load mismatch; (b) force-scaling rated load correction.

$$\begin{cases} F_{\text{pas}} = \sum_{n=0}^{N_q} q_n x^n \\ F_{\text{cor}} = \alpha \sum_{n=0}^{N_p} p_n x^n \\ F_c = \sum_{n=0}^{N_q} q_n x^n + \alpha \sum_{n=0}^{N_p} p_n x^n \end{cases} \tag{1}$$

wherein, F_{pas}, F_{cor}, and F_c denote the restoring forces of the passive QZS isolator, RLC, and QZS-RLC, respectively; q_n and p_n the polynomial fitting coefficients; N_p and N_q the polynomial order; x the displacement and α the scaling coefficient.

When the equilibrium positions of the passive QZS isolator and the RLC coincide at x_e, the rated load of the QZS-RLC can be calculated by

$$F_{ce} = F_{pe} + \alpha F_{re} = \sum_{n=0}^{N_q} q_n {x_e}^n + \alpha \sum_{n=0}^{N_p} p_n {x_e}^n \tag{2}$$

wherein, F_{pe} and F_{ce} denote the rated loads of the passive QZS isolator and QZS-RLC, respectively; F_{re} the rated load of the RLC when α=1.

In addition, one has

$$\begin{cases} k_c|_{x=x_e} = k_{ce} = k_{\text{pas}}|_{x=x_e} + \alpha k_{\text{cor}}|_{x=x_e} = k_{pe} + \alpha k_{re} \\ \dfrac{\mathrm{d}k_c}{\mathrm{d}x}\Big|_{x=x_e} = \dfrac{\mathrm{d}k_{\text{pas}}}{\mathrm{d}x}\Big|_{x=x_e} + \dfrac{\mathrm{d}k_{\text{cor}}}{\mathrm{d}x}\Big|_{x=x_e} = 0 \end{cases} \tag{3}$$

wherein, k_{pas}, k_{cor}, and k_c are the stiffnesses of the passive QZS isolator, RLC, and QZS-RLC, respectively; k_{pe} and k_{ce} the minimum stiffnesses at the equilibrium position of the passive QZS isolator and QZS-RLC, respectively; and k_{re} the minimum stiffness at the equilibrium position of the RLC when α=1.

It can be seen from Eq. (3) that the equilibrium position of the QZS-RLC retains at x_e. This indicates that the rated load of the passive QZS isolator can be continuously adjusted by scaling the rated load of the RLC while maintaining the equilibrium position unchanged. Hence, as shown in Fig. 1(d), load mismatch at point B can be eliminated to prevent performance degradation via force-scaling rated load correction. Moreover, when $k_{pe}F_{re}=k_{re}F_{pe}$, one has

$$\sqrt{\frac{k_{ce}}{F_{ce}}} = \sqrt{\frac{k_{pe}+\alpha k_{re}}{F_{pe}+\alpha F_{re}}} = \sqrt{\frac{k_{pe}}{F_{pe}}} \tag{4}$$

which indicates that the natural frequency remains constant when the rated load of the passive QZS isolator is adjusted through the proposed force-scaling rated load correction method.

2.2. Design of the rated load corrector

The force-scaling rated load correction method poses a prerequisite that the force-displacement curve of the rated load corrector should be scalable. According to electromagnetic theory, magnetic force is strongly dependent on current, enabling the development of an RLC to achieve a flexible scaling of the force-displacement curve. As illustrated in Fig. 2, for the purpose of validating the force-scaling rated load correction method, an RLC is designed, which consists of a permanent magnet, a negative-stiffness coil, a positive-stiffness coil, and a coil holder. Through electromagnetic interaction with the permanent magnet, the negative-stiffness coil generates negative stiffness, whereas the positive-stiffness coil generates positive stiffness. The negative-stiffness and the positive-stiffness coils are fixed to the coil holder, while the permanent magnet is movable. The permanent magnet and the positive-stiffness coil are arranged in an end-to-end configuration, while the magnet and the negative-stiffness coil are configured in a nested manner. By properly tuning the currents in the negative-stiffness and positive-stiffness coils, the RLC can achieve the QZS characteristic that is also scalable. As a result, when the RLC is configured in mechanical parallel with a passive QZS isolator, the system forms a parallel spring arrangement, allowing the rated load of the passive QZS isolator to be tuned via coil current. The passive QZS isolator presented in Fig. 2 has been described and developed in our previous work [53], referred to as the CCBS, and its structural design details are not repeated here.

To facilitate the alignment of the equilibrium positions between the passive QZS isolator and the RLC, the coil holder is attached to the frame via a threaded connection. By adjusting the screw-in length of the coil holder, the position of the RLC can be tuned to match the equilibrium positions of the RLC and the passive QZS isolator. In summary, implementing force-scaling rated load correction requires, first, the design of an RLC with a scalable force-displacement curve. Second, the RLC must be position-adjustable to align its equilibrium position with that of the passive QZS isolator. Additional requirements depend on the specific RLC design. For the proposed electromagnetic RLC, a magnet attached to the workload is necessary to enable electromagnetic interaction with the RLC. Moreover, it is worth highlighting that integrating the RLC with a passive QZS isolator is a reasonable and effective approach. Rated load correctors that may rely on external energy input often face limitations in achieving high load-bearing capacity due to energy consumption constraints. In contrast, passive QZS isolators offer excellent load-bearing performance but lack the ability to adjust the rated load, making them susceptible to performance degradation under load mismatch conditions. In practice, however, load variations are typically smaller than the rated load. Therefore, combining the RLC with a passive QZS vibration isolator enables a balanced design that enhances stability under load-varying operating conditions while maintaining strong practical applicability.

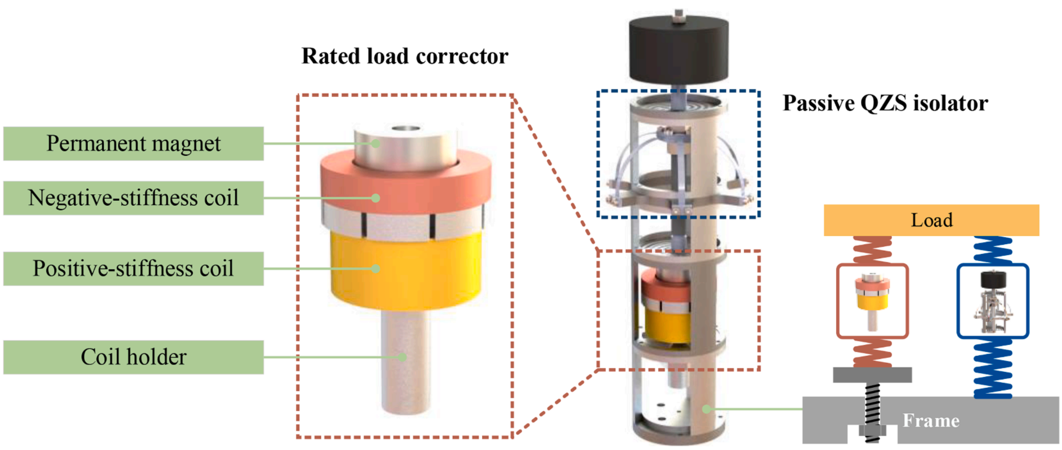

Fig. 2. Design of the rated load corrector and its application in a passive QZS isolator.

3. Implementation of the force-scaling rated load correction

3.1. Implementation of the force-scaling characteristic

The force-scaling characteristic is a prerequisite for implementing the force-scaling rated load correction. In this study, the positive correlation between the electromagnetic force and the input current is utilized as a representative case to achieve this characteristic. Based on the polarization current theory, the permanent magnet can be equivalently modeled as two thin-walled solenoids positioned on its inner and outer cylindrical surfaces respectively. Hence, the electromagnetic force between the permanent magnet and an energized coil is equal to the sum of the electromagnetic forces exerted between the coil and each of the thin-walled solenoids. As shown in Fig. 3(a, b), to calculate the electromagnetic force between the coil and the thin-walled solenoid, the filament method is adopted to uniformly divide the coil and the thin-walled solenoid into numerous coaxial wire loops.

As illustrated in Fig. 3(c), the position vectors of any point P_c on the coil wire loop and any point P_s on the solenoid wire loop can be expressed as

$$\begin{cases} \boldsymbol{R}_c = r_c\cos\varphi_c\boldsymbol{i} + r_c\sin\varphi_c\boldsymbol{j} + z_c\boldsymbol{k} \\ \boldsymbol{R}_s = r_s\cos\varphi_s\boldsymbol{i} + r_s\sin\varphi_s\boldsymbol{j} + z_s\boldsymbol{k} \end{cases} \tag{5}$$

wherein, r_c and z_c denote the radius and z coordinate of the coil wire loop, respectively; r_s and z_s the radius and z coordinate of the solenoid wire loop, respectively; φ_s the angle between the projection of $\boldsymbol{R}_s$ on the xoy plane and the x-axis and φ_c the angle between the projection of $\boldsymbol{R}_c$ on the xoy plane and the x-axis; $\boldsymbol{i}$, $\boldsymbol{j}$, and $\boldsymbol{k}$ are basis vectors.

According to Biot-Savart's law, the magnetic induction intensity generated by the current element at the point P_c is formulated as

$$\boldsymbol{B} = \frac{\mu_0}{4\pi}\oint\frac{I_c\mathrm{d}\boldsymbol{l}_c \times (\boldsymbol{R}_s - \boldsymbol{R}_c)}{|\boldsymbol{R}_s - \boldsymbol{R}_c|^3} \tag{6}$$

wherein, $I_c\mathrm{d}\boldsymbol{l}_c$ denotes the current element, $dl_c = -r_c\sin\varphi_c d\varphi_c i + r_c\cos\varphi_c d\varphi_c j$; I_c the current of the coil wire loop and μ_0 the vacuum permeability.

The magnetic flux density at the point P_s on the solenoid wire loop, generated by a single coil wire loop, can be expressed as

$$\begin{cases} B_x = \dfrac{\mu_0 I_c(z_s - z_c)\cos\varphi_s}{2\pi r_s\sqrt{r_s^2 + r_c^2 + (z_s - z_c)^2 + 2r_sr_c}}\left[\dfrac{r_s^2 + r_c^2 + (z_s - z_c)^2}{r_s^2 + r_c^2 + (z_s - z_c)^2 - 2r_cr_s}E(k) - F(k)\right] \\ B_y = \dfrac{\mu_0 I_c(z_s - z_c)\sin\varphi_s}{2\pi r_s\sqrt{r_s^2 + r_c^2 + (z_s - z_c)^2 + 2r_sr_c}}\left[\dfrac{r_s^2 + r_c^2 + (z_s - z_c)^2}{r_s^2 + r_c^2 + (z_s - z_c)^2 - 2r_cr_s}E(k) - F(k)\right] \\ B_z = \dfrac{\mu_0 I_c}{2\pi\sqrt{r_s^2 + r_c^2 + (z_s - z_c)^2 + 2r_sr_c}}\left[F(k) - \dfrac{r_s^2 + (z_s - z_c)^2 - r_c^2}{r_s^2 + r_c^2 + (z_s - z_c)^2 - 2r_cr_s}E(k)\right] \end{cases} \tag{7}$$

wherein, B_x, B_y, and B_z denote the magnetic flux density in the x, y, and z directions, respectively; F(k) and E(k) the elliptic integrals of the first and second kind respectively, and $k^2 = 4r_cr_s / \left[r_s^2 + r_c^2 + (z_s - z_c)^2 + 2r_cr_s\right]$.

According to Ampere's Law, the electromagnetic force acting on the current element $I_s\mathrm{d}\boldsymbol{l}_s$ at the point P_s is given as

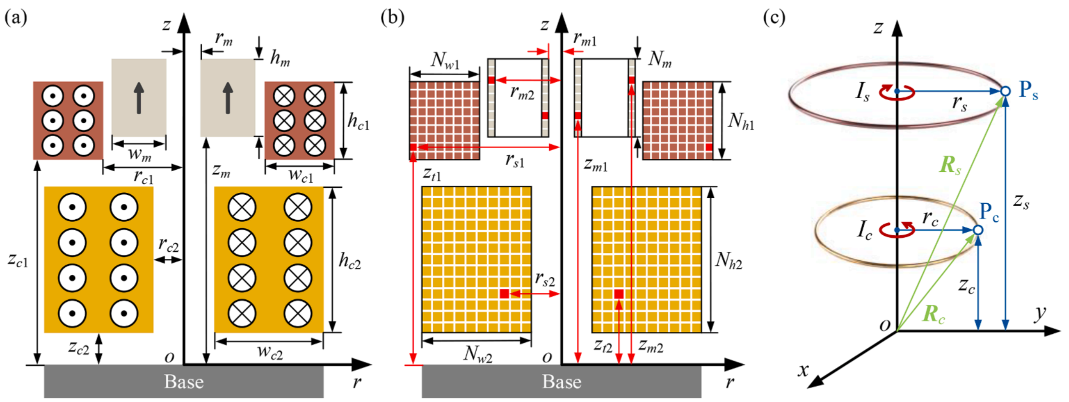

Fig. 3. Parameter definition of the permanent magnet, negative-stiffness coil, and positive-stiffness coil: (a) geometric parameter definition; (b) filament division; (c) electromagnetic force calculation between two coaxial wire loops.

$$\begin{aligned}\mathrm{d}\boldsymbol{F} &= I_s \mathrm{d}\boldsymbol{l}_s \times \boldsymbol{B} \\ &= -r_s I_s \cos\varphi_s B_z \mathrm{d}\varphi_s \boldsymbol{i} - r_s I_s \sin\varphi_s B_z \mathrm{d}\varphi_s \boldsymbol{j} - r_s I_s \left(B_y \sin\varphi_s + B_x \cos\varphi_s\right) \mathrm{d}\varphi_s \boldsymbol{k}\end{aligned} \tag{8}$$

wherein I_s denotes the current of the solenoid wire loop; $\mathrm{d}\boldsymbol{l}_s = -r_s \sin\varphi_s \mathrm{d}\varphi_s \boldsymbol{i} + r_s \cos\varphi_s \mathrm{d}\varphi_s \boldsymbol{j}$.

Since the coil wire loop and the solenoid coil wire loop are arranged coaxially, the electromagnetic force acting on the solenoid coil exists only in the z-axis. Integrating both sides of Eq. (8) gives

$$F_z = -\int_0^{2\pi} r_s I_s \left(B_y \sin\varphi_s + B_x \cos\varphi_s\right) \mathrm{d}\varphi_s = \frac{\mu_0 k I_c I_s (z_s - z_c)}{2\sqrt{r_c r_s}} \left[F(k) - \frac{2-k^2}{2-2k^2} E(k)\right] \tag{9}$$

The currents in the two thin-walled solenoids are equal in magnitude but flow in opposite directions, which can be calculated by

$$I_s = \frac{B_r h_m}{\mu_0 N_m} \tag{10}$$

wherein, B_r denotes the residual magnetic flux density of the permanent magnet; h_m the height of the permanent magnet and N_m the number of the wire loops.

As defined in Fig. 3(b), the radius and z coordinate of the p_i-th wire loop of the inner solenoid or the outer solenoid are calculated as

$$\begin{cases} r_s = r_{mi} = r_m + (i-1) w_m \\ z_s = z_{mi} = z_m + \left(p_i - \dfrac{1}{2}\right) \dfrac{h_m}{N_m} \qquad p_i \in [1, N_{\mathrm{m}}] \end{cases} \tag{11}$$

wherein, r_m and w_m denote the inner radius and width of the permanent magnet, respectively; z_m the z coordinate of the bottom surface of the permanent magnet; the subscript "i" the type of the solenoid, where $i = 1$ and $i = 2$ represent the inner and outer solenoids, respectively. The same convention applies to subsequent definitions of the subscript "i" and will not be repeatedly explained.

For the negative-stiffness and positive-stiffness coils, the radius and z coordinate of each wire loop can be expressed as

$$\begin{cases} r_c = r_{sj} = r_{cj} + \left(s - \dfrac{1}{2}\right) \dfrac{w_{cj}}{N_{wj}} \qquad s \in [1, N_{wj}] \\ z_c = z_{tj} = z_{cj} + \left(t - \dfrac{1}{2}\right) \dfrac{h_{cj}}{N_{hj}} \qquad t \in [1, N_{hj}] \end{cases} \tag{12}$$

wherein, r_c, w_c, and h_c denote the inner radius, width, and height of the coil, respectively; z_{cj} the z coordinate of the bottom surface of the coil; N_{wj} and N_{hj} the number of wire loops in the radial direction and the axial direction, respectively; the subscript "j" the type of the coil, where $j = 1$ and $j = 2$ represent the negative-stiffness coil and the positive-stiffness coil, respectively. The same convention applies to subsequent definitions of the subscript "j" and will not be reiterated.

The electromagnetic force of the RLC can be calculated by summing the interactions between each pair of wire loops, which is formulated as

$$F_{\mathrm{cor}} = \sum_{j=1}^{2} \sum_{i=1}^{2} \sum_{s=1}^{N_{wj}} \sum_{t=1}^{N_{hj}} \sum_{p_i=1}^{N_m} (-1)^i \frac{h_m I_{cj} B_r k_{ij} \left(z_{mi} - z_{tj}\right)}{2 N_m \sqrt{r_{sj} r_{mi}}} \left[F(k_{ij}) - \frac{2-k_{ij}^2}{2-2k_{ij}^2} E(k_{ij})\right] \tag{13}$$

wherein, I_{cj} denotes the current of the coil, and $k_{ij}^2 = 4 r_{sj} r_{mi} / \left[r_{sj}^2 + r_{mi}^2 + \left(z_{mi} - z_{tj}\right)^2 + 2 r_{sj} r_{mi}\right]$.

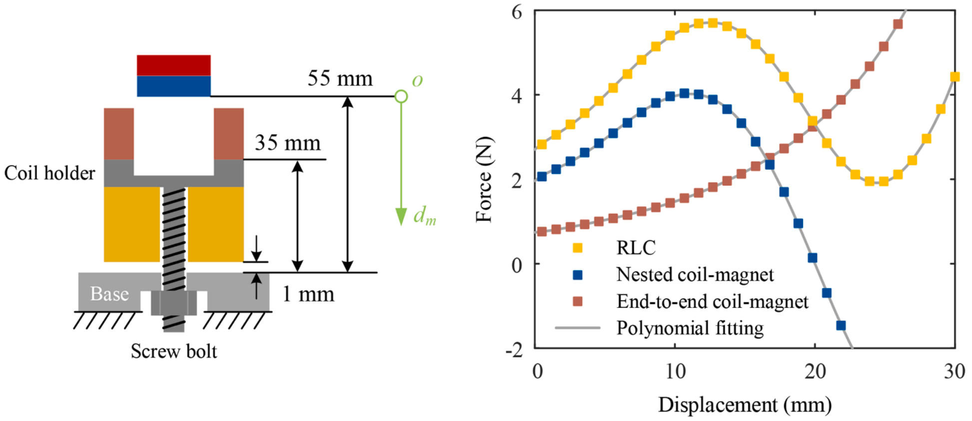

Fig. 4. Force-displacement curve of the nested coil-magnet, end-to-end coil-magnet, and RLC.

Fig. 4 plots the force-displacement curve of the nested coil-magnet, end-to-end coil-magnet, and RLC, where the negative-stiffness and positive-stiffness coils are fixed, and the permanent magnet is compressed toward the coils from z_m=55 mm. The remaining parameter settings are z_{c1}=35 mm, z_{c2}=1 mm, r_{c1}=19 mm, r_{c2}=9.5 mm, w_{c1}=11 mm, w_{c2}=17.5 mm, h_{c1}=12 mm, h_{c2}=25 mm, r_m=5 mm, w_m=13 mm, h_m=12 mm, N_{w1}=22, N_{w2}=35, N_{h1}= 24, N_{h2}=50, N_m=24, B_r=0.6 T, and I_{c1}=I_{c2}=1.0 A. It can be observed that the nested coil-magnet exhibits a negative stiffness characteristic, while the end-to-end coil-magnet demonstrates a hardening-stiffness behavior. Since the negative stiffness provided by the nested coil-magnet is much larger than the positive stiffness of the end-to-end coil-magnet, the electromagnetic force of the RLC initially increases and then decreases, further reflecting a negative stiffness characteristic. For facilitating the stiffness calculation of the RLC, the polynomial fitting Eq. (14) is harnessed to describe the force-displacement relationship of the RLC based on the discrete data obtained by Eq. (13). The polynomial order was selected appropriately to balance fitting accuracy, overfitting risk, nonlinear feature representation, and computational efficiency. The results obtained from Eqs. (13) and (14) show good agreement, without exhibiting noticeable oscillatory behavior.

$$F_{\text{cor}} = I_{c1}\sum_{r=0}^{9} q_r (d_m)^r + I_{c2}\sum_{r=0}^{7} p_r (d_m)^r \tag{14}$$

wherein, d_m denotes the displacement when the permeant magnet is compressed from z_m=55 mm; q_r and p_r fitting coefficients under I_{c1}=I_{c2}=1.0 A.

Defining the current ratio as I_r=I_{c2}/I_{c1}, Fig. 5(a, b) show the force-displacement and stiffness-displacement curves of the RLC, respectively, with the current in the positive-stiffness coil held constant as the current ratio I_r increases. When I_r=10/3, a QZS region appears on the force-displacement curve at a displacement of 17.93 mm, with a corresponding rated load of 0.33 kg and a minimum stiffness of 0.017 N/mm. In addition, it can be noted that the low-stiffness characteristic of the RLC can be flexibly tuned by varying the current ratio. Specifically, increasing the current ratio increases the stiffness, whereas decreasing it has the opposite effect.

At I_r=10/3, Fig. 6 plots the force-displacement and stiffness-displacement curves of the RLC under uniform scaling of coil currents ranging from 0.5 to 1.4 times their initial values. It is evident that both the force and stiffness scale proportionally, enabling effective adjustment of the rated load without altering the equilibrium position. Fig. 7 illustrates the equilibrium position adjustment of the RLC. By increasing the screw-in length of the coil holder by 5 mm, the z-coordinates of the bottom surfaces of both the positive- and negative-stiffness coils are raised by the same amount, resulting in a 5 mm leftward shift of the equilibrium position. Consequently, when the RLC is integrated with a passive QZS isolator, aligning their equilibrium positions through the equilibrium position adjustment of the RLC allows the rated load to be continuously tuned in real time through simple current tuning.

3.2. Rated load correction of the passive QZS isolator

The force-displacement curve of a passive QZS isolator can be fitted using a polynomial function. Without loss of generality, a third-degree polynomial $F_p = \sum_{r=0}^{3} s_r(d_m - d_s)^r$ is employed in this study. To correct the rated load of the passive QZS isolator, the RLC is required to be connected in parallel with it. As a consequence, the force-displacement relationship of the QZS-RLC can be described as

$$F_c = I_{c1}\sum_{r=0}^{9} q_r (d_m + d_t)^r + I_{c2}\sum_{r=0}^{7} p_r (d_m + d_t)^r + \sum_{r=0}^{3} s_r (d_m - d_s)^r \tag{15}$$

wherein, d_t denotes the variation in the screw-in length of the coil holder, with d_t=0 corresponding to the reference QZS configuration shown in Fig. 6; d_s the equilibrium position of the passive QZS isolator and s_r the fitting coefficients.

Fig. 8 presents the force-displacement and stiffness-displacement curves of the RLC, passive QZS isolator, and QZS-RLC, where the

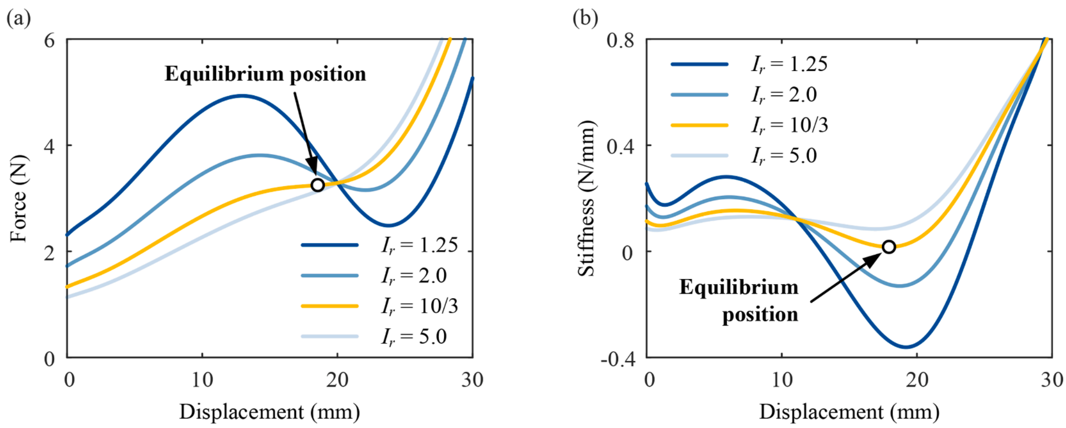

Fig. 5. Force-displacement and stiffness-displacement curves of the RLC as the current ratio increases: (a) force-displacement curves; (b) stiffness-displacement curves.

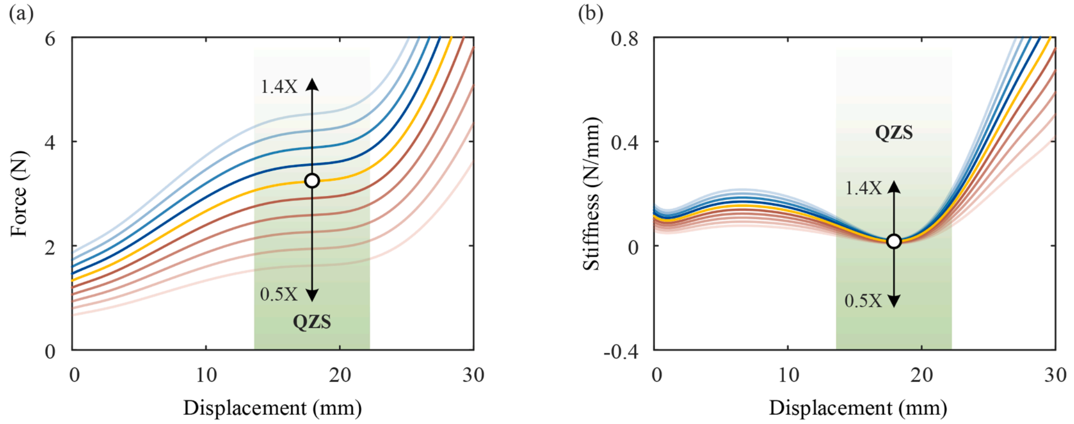

Fig. 6. Scaling characteristics achieved through simple current tuning: (a) force scaling; (b) stiffness scaling.

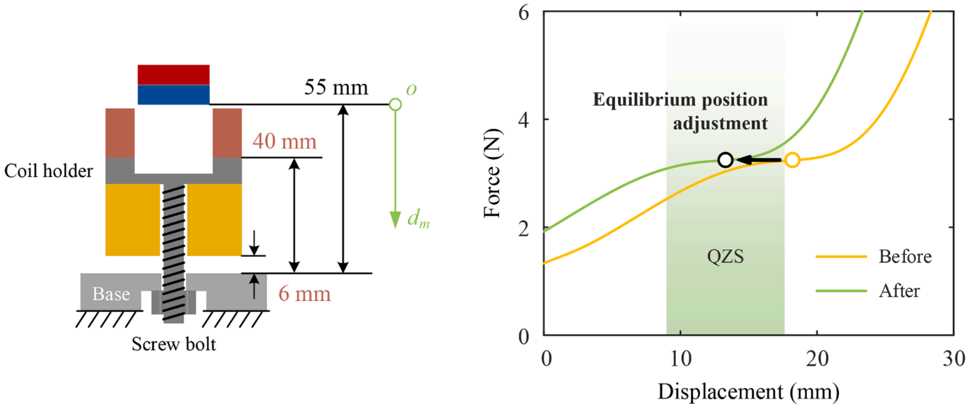

Fig. 7. Equilibrium position adjustment of the RLC.

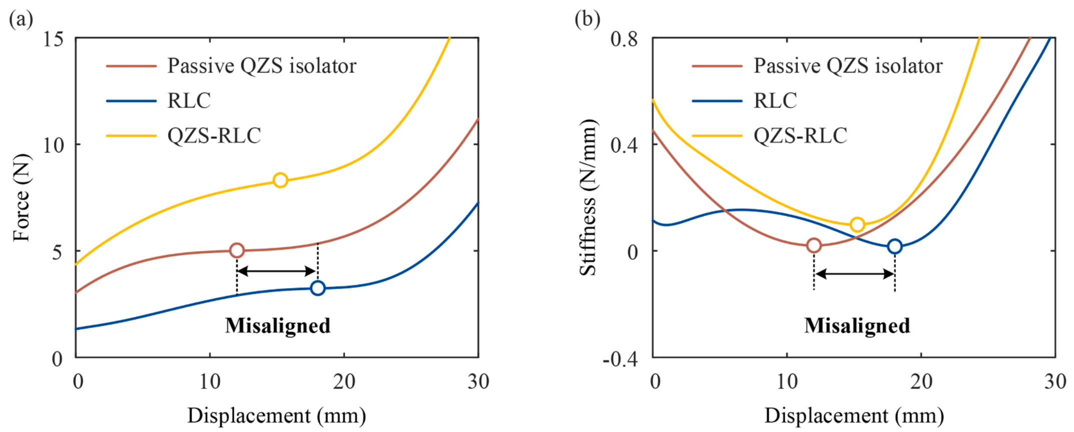

Fig. 8. Force-displacement and stiffness-displacement curves of the RLC, passive QZS isolator, and QZS-RLC under misaligned configuration: (a) force-displacement curves; (b) stiffness-displacement curves.

parameter settings are d_t=0 mm, d_s=12 mm, s_0=5.0 N, s_1=0.02 N/mm, s_2=0 N/mm^2, and s_3=0.001 N/mm^3. The equilibrium position of the passive QZS isolator is located at a displacement of 12 mm, corresponding to a rated load of 0.51 kg and a minimum stiffness of 0.02 N/mm. Apparently, the equilibrium positions of the passive QZS isolator and the RLC are misaligned. The force-displacement and stiffness-displacement curves of the QZS-RLC are obtained by superimposing those of the RLC and passive QZS isolator. At the displacement of 12 mm, although the passive QZS isolator exhibits minimum stiffness, the RLC possesses a relatively higher positive stiffness at the same position. Similarly, at the displacement of 17.93 mm, the QZS characteristic of the RLC is degraded due to the influence of the passive QZS isolator. As a result, the QZS-RLC fails to exhibit a desired QZS region. Since the force-displacement curves of both the RLC and the passive QZS isolator are monotonic, their superimposed curve rises with displacement. Furthermore, owing to the softening-to-hardening transition behavior around the equilibrium positions of both the RLC and the passive QZS isolator, the superimposed curve displays a similar characteristic, with the position of minimum stiffness occurring between the equilibrium positions of the two systems.

Fig. 9 shows the equilibrium position alignment process of the RLC and passive QZS isolator. As shown in Fig. 9(a), increasing d_t causes the equilibrium position of the RLC to gradually approach that of the passive QZS isolator. Meanwhile, the position of minimum stiffness of the QZS-RLC also shifts toward the equilibrium position of the passive QZS isolator. When d_t=5.93 mm, the equilibrium positions of the RLC, passive QZS isolator, and QZS-RLC become fully aligned. As illustrated in Fig. 9(b), the minimum stiffness of the QZS-RLC decreases progressively with increasing d_t, reaching its lowest value at d_t=5.93 mm. In the aligned configuration, due to the superposition effect, the rated load and stiffness of the QZS-RLC equal the sum of those of the passive QZS isolator and the RLC.

Under the aligned configuration, the rated load of the passive QZS isolator can be flexibly adjusted via force-scaling rated load correction. As shown in Fig. 10(a), with I_r=10/3 kept constant, uniformly scaling the coil currents by the same factor proportionally scales the rated load of the RLC. Owing to the superposition effect, the rated load of the QZS-RLC can thus be flexibly varied, in contrast to the fixed rated load of the passive QZS isolator. For example, under the initial configuration with I_{c1}=0.3 A and I_{c2}=1.0 A, the rated loads of the RLC and QZS-RLC are 0.33 kg and 0.84 kg, respectively. When the currents are scaled by a factor of 1.4 (denoted as 1.4X) to I_{c1}=0.42 A and I_{c2}=1.4 A, the rated load of the RLC increases to 0.46 kg, and that of the QZS-RLC is successfully corrected to 0.97 kg. It is worth noting that scaling the rated load simultaneously alters the stiffness characteristic of the RLC, thereby modifying the stiffness of the QZS-RLC as well, as shown in Fig. 10(b). This coupling effect is advantageous, as the concurrent variation in rated load and stiffness helps maintain a stable natural frequency and thus ensures consistent low-frequency vibration isolation performance.

4. Static comparison with conventional rated load adjustment

In conventional QZS isolators, the bistable negative stiffness is employed to counteract the linear positive stiffness, while the applied load is primarily supported by the linear positive-stiffness element. Therefore, rated load adjustment can be achieved by tunning the compression of this linear element. Assuming the stiffness of the linear positive-stiffness element is k_l=0.5 N/mm, the force-displacement relationship of the bistable negative-stiffness element can then be expressed as $F_b = \sum_{r=0}^{3} s_r(d_m - d_s)^r - k_l(d_m - d_s + s_0/k_l)$. Considering the adjustable compression of the linear positive-stiffness element. The force-displacement relationship of a conventional QZS isolator can be expressed as

$$F_b = \sum_{r=0}^{3} s_r(d_m - d_s)^r - k_l(d_m - d_s + s_0 / k_l) + k_l d_l \tag{16}$$

wherein, d_l denotes the variation in compression of the linear positive-stiffness element.

With the fitting coefficients set as s_0=10.0 N, s_1=0.04 N/mm, s_2=0 N/mm^2, and s_3=0.001 N/mm^3, the linear positive-stiffness element exhibits a compression of 20 mm, as shown in Fig. 11(a). Under this condition, the QZS isolator possesses a rated load of 1.02 kg and a minimum stiffness of 0.04 N/mm at an equilibrium position of 12 mm. As d_l decreases, the compression of the linear positive-stiffness element required to reach the equilibrium position decreases, thereby reducing the rated load. Specifically, as d_l decreases from 0 mm to −10 mm, the rated load drops from 1.02 kg to 0.51 kg. Unlike the force-scaling rated load correction method, as shown in Fig. 11(b), adjusting the compression of the linear positive-stiffness element has no effect on the stiffness characteristic.

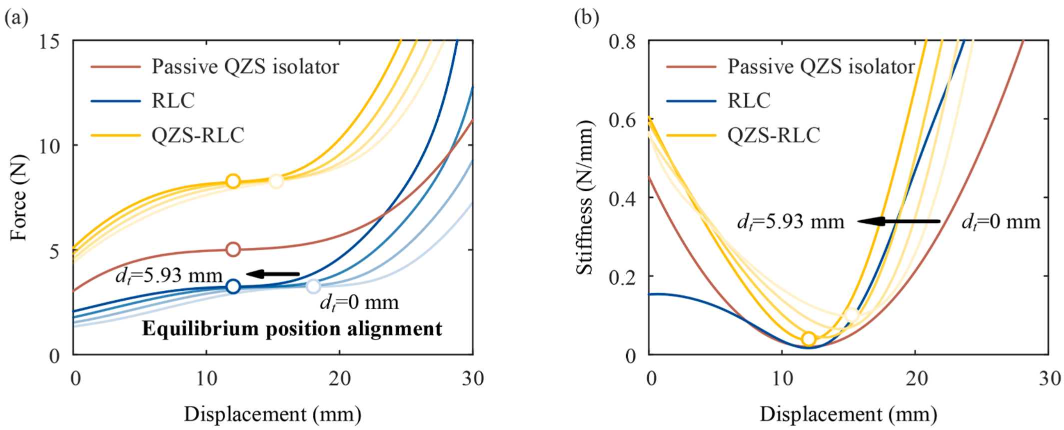

Fig. 9. Force-displacement and stiffness-displacement curves of the RLC, passive QZS isolator, and QZS-RLC during the equilibrium position alignment process: (a) force-displacement curves; (b) stiffness-displacement curves.

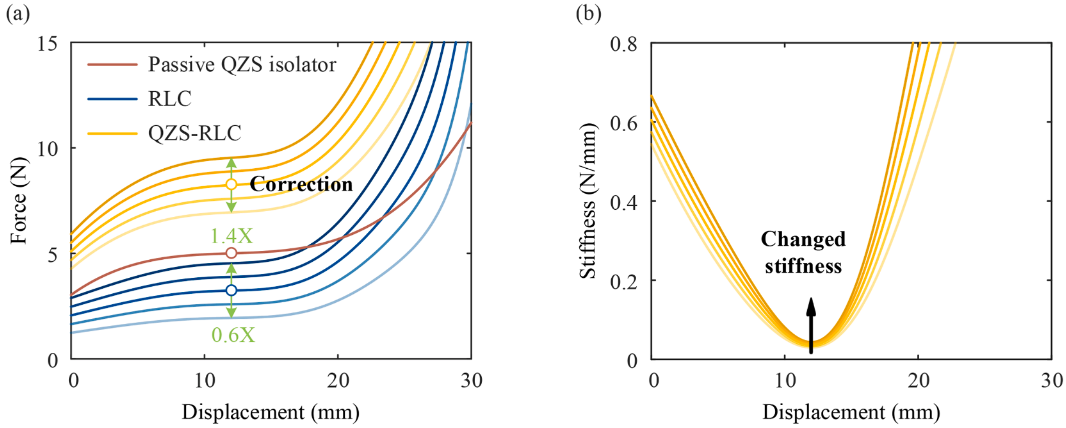

Fig. 10. Force-displacement and stiffness-displacement curves under force-scaling rated load correction: (a) force-displacement curves of the RLC, passive QZS isolator, and QZS-RLC; (b) stiffness-displacement curves of the QZS-RLC.

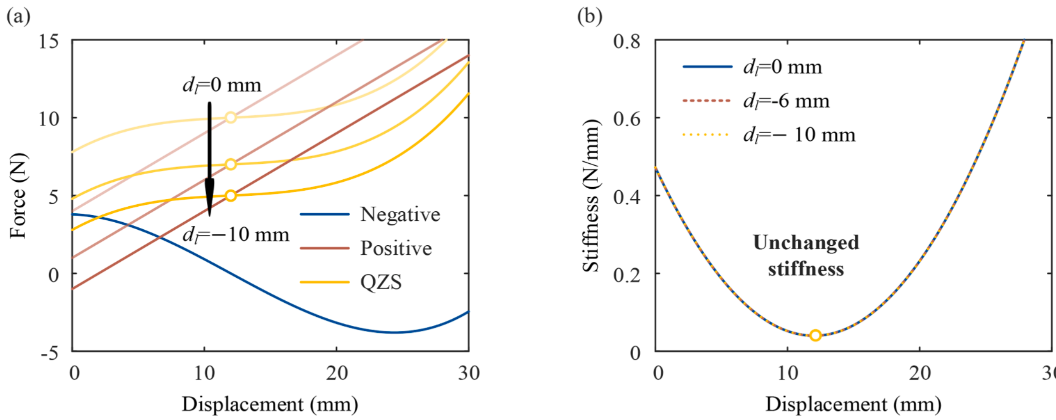

Fig. 11. Force-displacement and stiffness-displacement curves under conventional rated load correction: (a) force-displacement curves of the bistable negative-stiffness element, linear positive-stiffness element, and conventional QZS isolator; (b) stiffness-displacement curves of the conventional QZS isolator.

Detrimentally, when the rated load decreases from 1.02 kg to 0.51 kg, the natural frequency of the QZS isolator increases from 1.0 Hz to 1.41 Hz. The coupling between the rated load and natural frequency can result in unstable low-frequency vibration isolation performance.

Importantly, the force-scaling rated load correction method is capable of maintaining a constant natural frequency while correcting the rated load. To achieve this, the rated loads and minimum stiffnesses of the passive QZS isolator and the RLC are required to satisfy

$$\sqrt{\frac{k_{pe}+k_{re}}{m_{pe}+m_{re}}}=\sqrt{\frac{k_{pe}+\alpha k_{re}}{m_{pe}+\alpha m_{re}}} \tag{17}$$

wherein, m_{pe} and m_{re} denote the rated loads of the passive QZS isolator and RLC, respectively.

Derived from Eq. (17), we can obtain

$$f_{pe}=f_{re}=\frac{1}{2\pi}\sqrt{\frac{k_{pe}}{m_{pe}}}=\frac{1}{2\pi}\sqrt{\frac{k_{re}}{m_{re}}} \tag{18}$$

wherein, f_{pe} and f_{re} denote the natural frequencies of the passive QZS isolator and RLC, respectively.

Eq. (18) demonstrates that when the natural frequencies of the RLC and the passive QZS isolator are identical, the QZS-RLC is capable of maintaining a constant natural frequency during rated load correction. As discussed in Section 3.2, the rated load and minimum stiffness of the RLC can be readily adjusted by varying the current configuration to obtain the target natural frequency. For a given passive QZS isolator, we have

$$\begin{cases} m_{pe}g = I_{c1}\sum_{r=0}^{9} q_r(d_{re})^r + I_{c2}\sum_{r=0}^{7} p_r(d_{re})^r \\ k_{pe} = I_{c1}\sum_{r=1}^{9} rq_r(d_{re})^{r-1} + I_{c2}\sum_{r=1}^{7} rp_r(d_{re})^{r-1} \\ 0 = I_{c1}\sum_{r=2}^{9} r(r-1)q_r(d_{re})^{r-2} + I_{c2}\sum_{r=2}^{7} r(r-1)p_r(d_{re})^{r-2} \end{cases} \tag{19}$$

wherein, d_{re} denotes the equilibrium position of the RLC.

Derived from Eq. (19), the corresponding current ratio can be determined by solving

$$\begin{cases} f_{pe} = \dfrac{1}{2\pi}\sqrt{\dfrac{\sum_{r=1}^{9} rq_r(d_{re})^{r-1} + I_r\sum_{r=1}^{7} rp_r(d_{re})^{r-1}}{\left[\sum_{r=0}^{9} q_r(d_{re})^r + I_r\sum_{r=0}^{7} p_r(d_{re})^r\right]}g} \\ I_r = -\dfrac{\sum_{r=2}^{9} r(r-1)q_r(d_{re})^{r-2}}{\sum_{r=2}^{7} r(r-1)p_r(d_{re})^{r-2}} \end{cases} \tag{20}$$

Once the current ratio I_r is determined, the current configuration corresponding to a prescribed rated load of the RLC can be calculated as

$$\begin{cases} I_{c1} = \dfrac{m_{re}g}{\sum_{r=0}^{9} q_r(d_{re})^r + I_r\sum_{r=0}^{7} p_r(d_{re})^r} \\ I_{c2} = \dfrac{m_{re}gI_r}{\sum_{r=0}^{9} q_r(d_{re})^r + I_r\sum_{r=0}^{7} p_r(d_{re})^r} \end{cases} \tag{21}$$

As a case study, the polynomial fitting coefficients of the passive QZS isolator are set as s_0=5.0 N, s_1=0.02 N/mm, s_2=0 N/mm^2, and s_3=0.001 N/mm^3, with a natural frequency of 1.0 Hz. To enable the QZS-RLC system to achieve a rated load of 1.02 kg while maintaining the same natural frequency, the desired parameters for the RLC are specified as m_{re}=0.51 kg and k_{re}=0.02 N/mm, sharing the same natural frequency as the passive QZS isolator. Based on Eq. (19), the calculated values are d_{re}=17.97 mm, I_r=3.275, I_{c1}=0.471 A, and I_{c2}=1.541 A. Fig. 12 presents the force-displacement and stiffness-displacement curves of the passive QZS isolator, RLC, and QZS-RLC. Under the parameter configuration derived from Eq. (19), the equilibrium position of the RLC is located at a displacement of 17.97 mm, corresponding to a rated load of 0.51 kg and a minimum stiffness of 0.02 N/mm. After performing equilibrium position adjustment, the equilibrium position of the RLC is shifted to 12 mm when d_t=5.97 mm, aligning it with that of the passive QZS isolator. With the assistance of the RLC, the rated load of the QZS-RLC reaches the prescribed value. Interestingly, as shown in Fig. 13, when the rated load is adjusted using the force-scaling rated load correction method, the natural frequency of the QZS-RLC remains constant at 1.0 Hz. For instance, when α=0.2, the rated load of the QZS-RLC reduces to 0.61 kg, and the corresponding minimum stiffness

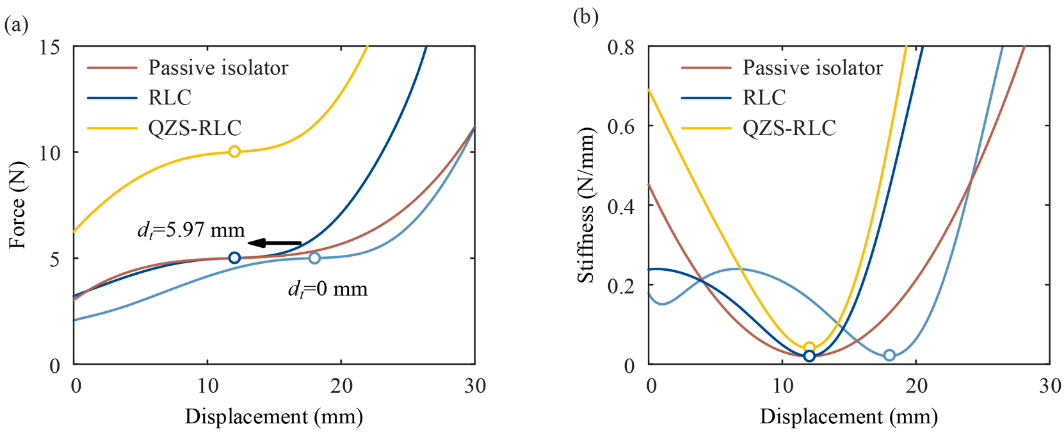

Fig. 12. Rated load adjustment without altering the natural frequency through force-scaling rated load correction: (a) force-displacement curves; (b) stiffness-displacement curves.

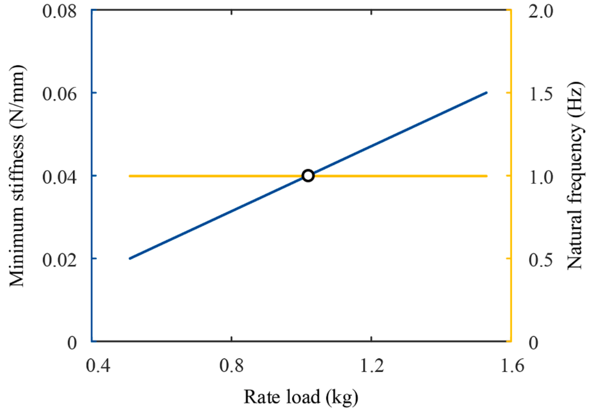

Fig. 13. Variation in the minimum stiffness and natural frequency of the QZS-RLC under force-scaling rated load correction.

increases to 0.024 N/mm, while the natural frequency remains unchanged at 1.0 Hz. This characteristic ensures stable low-frequency vibration isolation performance.

Considering that the equilibrium positions of the passive QZS isolator and the RLC may not be perfectly aligned in practical applications, Fig. 14(a) illustrates the force-displacement curves of the QZS-RLC under different values of d_t. It can be observed that such misalignment causes the actual operating position to deviate from the desired equilibrium position. Fig. 14(b) further presents the stiffness and natural frequency of the QZS-RLC at the actual operating position as d_t varies. In the presence of misalignment, the stiffness increases and deviates from the desired value, leading to a rise in the natural frequency and, consequently, a degradation in isolation performance. The greater the misalignment, the more pronounced the performance degradation. Nevertheless, it is worth emphasizing that when misalignment occurs, the workload shifts away from the prescribed equilibrium position. This characteristic makes the misalignment readily detectable and, therefore, avoidable through direct observation of the workload position.

5. Dynamic comparison with the conventional rated load correction

5.1. Dynamic modeling considering rated load correction

For facilitating dynamic modeling, under the aligned configuration in Fig. 12(a), a coordination transformation is conducted by defining the equilibrium position as the displacement origin. Fifth-order polynomial fitting, considering both the force-scaling rated load correction and conventional rated load correction, is used to recharacterize the force-displacement relationships of the RLC and passive QZS isolator. As plotted in Fig. 15, the fitting results closely match the experimental data with root-mean-square errors below 0.003 N. As a consequence, the force-displacement relationship of the QZS-RLC can be reformulated as

$$F_c = F_{\mathrm{cor}} + F_{\mathrm{pas}} = \frac{I_t}{I_{c10} + I_{c20}} \sum_{r=0}^{5} v_r z^r + \sum_{r=0}^{5} w_r z^r + k_l d_l \tag{22}$$

wherein, z=d_m−d_s; v_r denotes the fitting coefficients of the RLC under the initial current configuration I_{c10}=0.471 A and I_{c20}=1.541 A; w_r the fitting coefficients of the passive QZS isolator; I_t= I_{c2}+I_{c1}, and I_r=3.275.

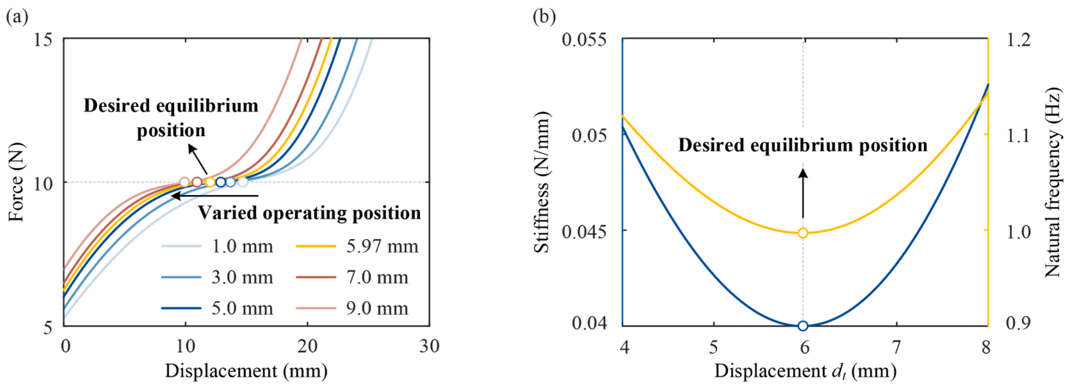

Fig. 14. Effects of misalignment between the equilibrium positions of the passive QZS isolator and the RLC: (a) variation in the actual operating position; (b) variations in the stiffness and natural frequency of the QZS-RLC.

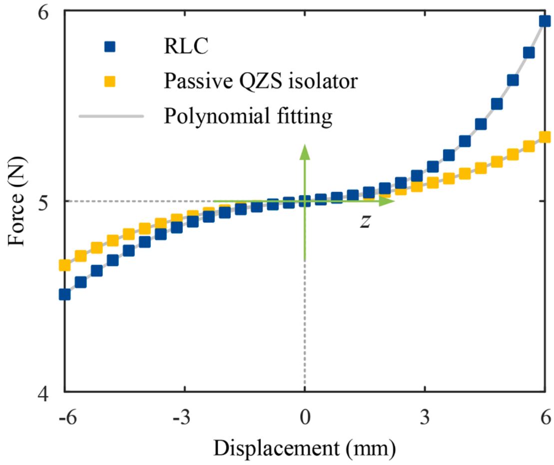

Fig. 15. Coordination transformation with the equilibrium position defined as the displacement origin.

Fig. 16 depicts a single-degree-of-freedom model of the QZS-RLC, comprising a lumped mass element m, the nonlinear stiffness units k_{cor} and k_{pas} elements (derived from the RLC and passive QZS isolator, respectively), and a damping element c that primarily accounts for electromagnetic damping and aerodynamic drag. Hence, when the QZS-RLC is disturbed by the base excitation z_b, the dynamic governing equation can be expressed as

$$\ddot{z} + 2\zeta\omega_0(\dot{z} - \dot{z}_b) + \frac{I_t}{m(I_{c10} + I_{c20})}\sum_{r=0}^{5} v_r(z - z_b)^r + \frac{1}{m}\sum_{r=0}^{5} w_r(z - z_b)^r + \frac{k_l d_l}{m} - g = 0 \tag{23}$$

wherein, ζ denotes the damping coefficient, and $\zeta = c/(2m\omega_0)$; $\omega_0 = \sqrt{[v_1 I_t/(I_{c10} + I_{c20}) + w_1]/m}$; g the gravitational acceleration constant, and $g = 9.81$ m/s^2.

Assume z_b=$a_b$cos(ωt), where a_b is the excitation amplitude and ω is the angular frequency. According to the Harmonic Balance Method, the relative displacement response of the mass element can be assumed as z_r=a_0+$a_1$cos(ωt+φ), where a_0, a_1, and φ are the amplitude, offset, and phase, respectively. Substituting the expressions of z_r and z_b into Eq. (23) yields

$$\begin{aligned} &\bar{p}_1 a_0 + \bar{p}_2\left(a_0{}^2 + \frac{a_1{}^2}{2}\right) + \bar{p}_3\left(a_0^3 + \frac{3}{2}a_0 a_1^2\right) + \bar{p}_4\left(a_0{}^4 + 3a_0{}^2 a_1{}^2 + \frac{3}{8}a_1{}^4\right) \\ &+\bar{p}_5\left(a_0^5 + 5a_0^3 a_1^2 + \frac{15}{8}a_0 a_1^4\right) + \bar{p}_0 = 0 \end{aligned} \tag{24}$$

$$\begin{cases} \begin{bmatrix} -a_1\omega^2 + \bar{p}_1 a_1 + 2\bar{p}_2 a_0 a_1 + \bar{p}_3\left(3a_0{}^2 a_1 + \dfrac{3}{4}a_1{}^3\right) \\ +\bar{p}_4\left(4a_0{}^3 a_1 + 3a_0 a_1{}^3\right) \\ +\bar{p}_5\left(5a_0{}^4 a_1 + \dfrac{15}{2}a_0{}^2 a_1{}^3 + \dfrac{5}{8}a_1{}^5\right) \end{bmatrix}\cos\varphi - 2a_1\zeta\omega\omega_0\sin\varphi = a_b\omega^2 \\ \begin{bmatrix} -a_1\omega^2 + \bar{p}_1 a_1 + 2\bar{p}_2 a_0 a_1 + \bar{p}_3\left(3a_0{}^2 a_1 + \dfrac{3}{4}a_1{}^3\right) \\ +\bar{p}_4\left(4a_0{}^3 a_1 + 3a_0 a_1{}^3\right) \\ +\bar{p}_5\left(5a_0{}^4 a_1 + \dfrac{15}{2}a_0{}^2 a_1{}^3 + \dfrac{5}{8}a_1{}^5\right) \end{bmatrix}\sin\varphi + 2a_1\zeta\omega\omega_0\sin\varphi = 0 \end{cases} \tag{25}$$

wherein, $\bar{p}_0 = [v_0 I_t/(I_{c10} + I_{c20}) + w_0 + k_l d_l]/m - g$; $\bar{p}_i = I_t v_i/[m(I_{c10} + I_{c20})] + w_i/m$, and $i = 1, 2, 3, 4, 5$.

Derived from Eq. (25), we can obtain

$$\begin{bmatrix} -a_1\omega^2 + \bar{p}_1 a_1 + 2\bar{p}_2 a_0 a_1 + \bar{p}_3\left(3a_0{}^2 a_1 + \dfrac{3}{4}a_1{}^3\right) \\ +\bar{p}_4\left(4a_0{}^3 a_1 + 3a_0 a_1{}^3\right) + \bar{p}_5\left(5a_0{}^4 a_1 + \dfrac{15}{2}a_0{}^2 a_1{}^3 + \dfrac{5}{8}a_1{}^5\right) \end{bmatrix}^2 + (2a_1\zeta\omega\omega_0)^2 = (a_b\omega^2)^2 \tag{26}$$

By combining Eqs. (26) and (24), the parameters a_0, a_1, and φ can be calculated, and the absolute displacement response of the mass

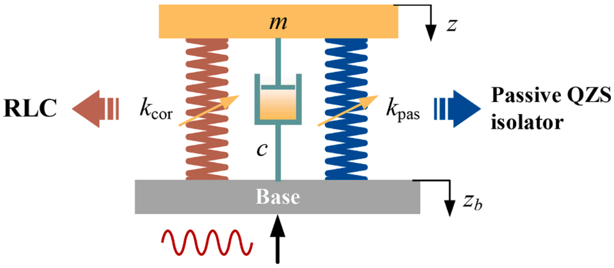

Fig. 16. A single-degree-of-freedom model of the QZS-RLC.

element can be expressed as

$$z = z_b + z_r = a_b\cos(\omega t) + a_0 + a_1\cos(\omega t + \varphi) \tag{27}$$

5.2. Dynamic behavior without rated load correction

The dynamic behavior of the QZS-RLC is characterized by displacement transmissibility, which can be calculated by

$$T_d = 20\lg\left(\frac{1}{a_b}\sqrt{{a_1}^2 + {a_b}^2 + 2a_1a_b\cos\varphi}\right) \tag{28}$$

The parameters of the QZS-RLC are set as I_t=I_{c10}+I_{c20}, k_l=0.5 N/mm, d_l=0 mm, m = 1.02 kg, and ζ=0.0783, ensuring that the QZS-RLC operates without load mismatch. Fig. 17(a) presents the displacement transmissibility curve under an excitation amplitude a_b=0.5 mm. Overall, due to the hardening nonlinearity, the resonance peak of the transmissibility curve bends significantly to the right, resulting in a bifurcation behavior in the frequency range from 1.3 Hz to 1.8 Hz. This region exhibits three solution branches: an upper branch, a lower branch, and a middle branch. The upper and lower branches correspond to stable responses, while the middle branch is unstable. When the excitation frequency increases from low to high, the system follows the upper branch, with transmissibility gradually rising to a peak of 21.2 dB, then abruptly jumping down to −6.4 dB at 1.8 Hz. Conversely, when the excitation frequency decreases from high to low, the system follows the lower branch, with transmissibility gradually increasing to 9.1 dB, then suddenly jumping up to 17.2 dB at 1.3 Hz. Define the frequency at which the transmissibility first drops below 0 dB as the starting isolation frequency. Fig. 17(b) shows the displacement transmissibility curves under different damping conditions. It can be seen that the jump phenomenon in the transmissibility curve increases the starting isolation frequency from 1.5 Hz to 1.8 Hz, thereby narrowing the isolation bandwidth. When the damping coefficient is increased from ζ=0.0783 to ζ=0.1018, the jump behavior is completely suppressed, and the starting isolation frequency returns to 1.5 Hz. Further increasing the damping to ζ=0.1409 eliminates the bifurcation characteristics in the transmissibility curve. The numerical results obtained using the Runge-Kutta Method (RKM) are also plotted, and the data points closely follow the theoretical curve, confirming the effectiveness of the dynamic model. However, raising the damping coefficient can weaken the vibration attenuation within the isolation region. For instance, when the damping coefficient increases from ζ=0.0783 to ζ=0.1409, the transmissibility rises from −22.0 dB to −19.9 dB at 4 Hz. As a result, the damping should be properly chosen to balance vibration suppression and mitigate the influence of stiffness nonlinearity on the performance of the QZS isolator.

Keeping the parameters of the QZS-RLC identical to those in Fig. 17(a) except for the applied load, Fig. 18(a, b) respectively show the offset curves and displacement transmissibility curves under different load mismatches. The applied load is set as 1.02 kg, 0.99 kg, and 0.94 kg in sequence. When the applied load equals the rated load, the QZS-RLC operates at its equilibrium position, resulting in a

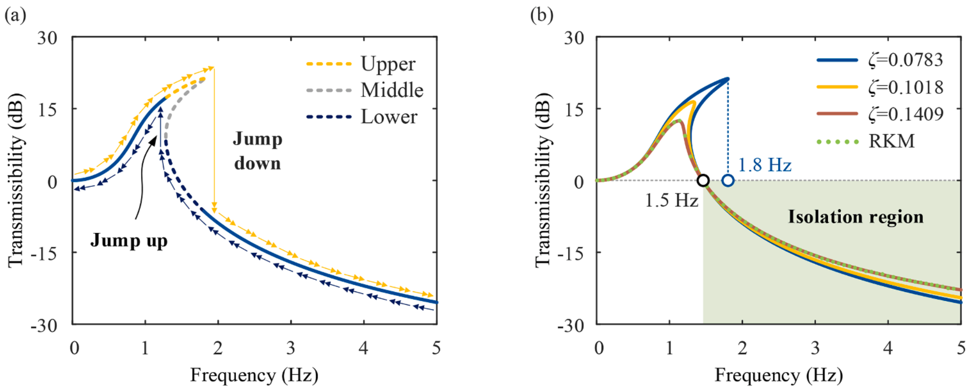

Fig. 17. Displacement transmissibility curves without load mismatch: (a) bifurcation behavior; (b) transmissibility curves under different damping conditions.

minimal offset. Due to its low dynamic stiffness, neglecting the jump phenomenon, the QZS-RLC exhibits a low starting isolation frequency of 1.5 Hz. As the applied load decreases, the stiffness nonlinearity causes the operating position to deviate from the equilibrium position, leading to a sharp increase in the offset and, consequently, in the dynamic stiffness. As a result, the starting isolation frequency increases significantly, and ultra-low frequency isolation performance deteriorates. For instance, when the applied load decreases slightly from the rated load to 0.99 kg, a load mismatch of only 2.9% (30 g) leads to a 290% rise in dynamic stiffness and an 86.7% increase in the starting isolation frequency. Furthermore, when the applied load decreases to 0.99 kg, the resonance peak initially tilts to the left and then bends to the right, showing a complex dynamic behavior with initial softening followed by hardening. As the applied load further decreases to 0.94 kg, the resonance peak exhibits a pronounced leftward tilt. These results demonstrate that load mismatch disrupts the ultra-low-stiffness characteristic of the QZS-RLC, increases the starting isolation frequency, amplifies stiffness nonlinearity effects, and severely degrades low-frequency isolation performance. In extreme cases, such a mismatch may even induce complex dynamic phenomena and lead to isolator instability. Therefore, a QZS isolator can only achieve optimal low-frequency isolation performance when operating under its rated load.

5.3. Dynamic behavior with rated load correction

The conventional rated load correction is first applied to eliminate load mismatches. The initial rated load is set to 1.02 kg. When the applied load is adjusted to 0.99 kg, 0.94 kg, and 0.62 kg, the corresponding compression changes of the linear positive-stiffness element are set to d_l=−0.59 mm, d_l=−1.57 mm, and d_l=−6.08 mm, respectively, to match the rated load with the applied load. Fig. 19 presents the offset and transmissibility curves under conventional rated load correction. As shown in Fig. 19(a), as the applied load increases, the static operating position coincides with the equilibrium position, and the offset remains as low as that at the initial rated load. Fig. 19(b) shows that under small variations in the applied load, the transmissibility curves change negligibly, indicating that the conventional rated load correction effectively eliminates load mismatches while having little influence on the vibration isolation performance. However, when the applied load decreases from 1.02 kg to 0.62 kg (a 39.2% reduction), the resonance region shifts to a higher frequency, and the starting isolation frequency increases from 1.5 Hz to 1.9 Hz when neglecting the jump phenomenon, revealing a clear degradation in low-frequency vibration isolation performance. In addition, the transmissibility peak decreases with the reduction of the applied load. These results can be attributed to the fact that the conventional rated load correction does not alter the stiffness characteristics. As a result, as the applied load decreases, both the natural frequency and damping coefficient increase, leading to a higher starting isolation frequency and a lower peak transmissibility.

Under the force-scaling rated load correction, for the applied loads of 0.99 kg, 0.94 kg, and 0.62 kg, the corresponding current configurations are I_t=1.894 A, 1.696 A, and 0.433 A, respectively, ensuring consistency between the rated and applied loads. As shown in Fig. 20(a), the offset curves demonstrate that by tuning the rated load of the RLC, the load mismatches are effectively eliminated and the offset is maintained at a low level. Significantly, as plotted in Fig. 20(b), in drastic contrast to the conventional rated load correction, the resonance region remains fixed owing to the constant natural frequency, thereby ensuring a stable starting isolation frequency. This advantage persists even under a 39.2% reduction in the initial rated load and becomes more pronounced as the reduction increases. In addition, as the applied load decreases, the damping coefficient increases as the conventional rated load correction, leading to a similar variation in the transmissibility curves as observed in Fig. 17(b). However, in a different manner, during the force-scaling rated load correction, there is $\zeta \propto m$, whereas under the conventional rated load correction, there is $\zeta \propto \sqrt{m}$.

However, in practical applications, force-scaling rated load correction may be imperfect due to mismatches in the natural frequencies between the RLC and the passive QZS isolator. Maintaining the natural frequency of the passive QZS isolator unchanged as f_{pe}=1.0 Hz, Figs. 21 and 22 plot the transmissibility curves for cases where f_{re}>f_{pe} and f_{re}<f_{pe}, respectively. In Fig. 21(a), the desired stiffness of the RLC is raised to 0.06 N/mm, which results in a natural frequency of 1.73 Hz. The corresponding current settings are I_r=3.711, I_{c10}=0.424 A, and I_{c20}=1.573 A. Compared with the perfect case, the increased natural frequency of the RLC, resulting from enhanced stiffness, shifts the resonance region toward higher frequencies, thereby degrading the low-frequency vibration isolation

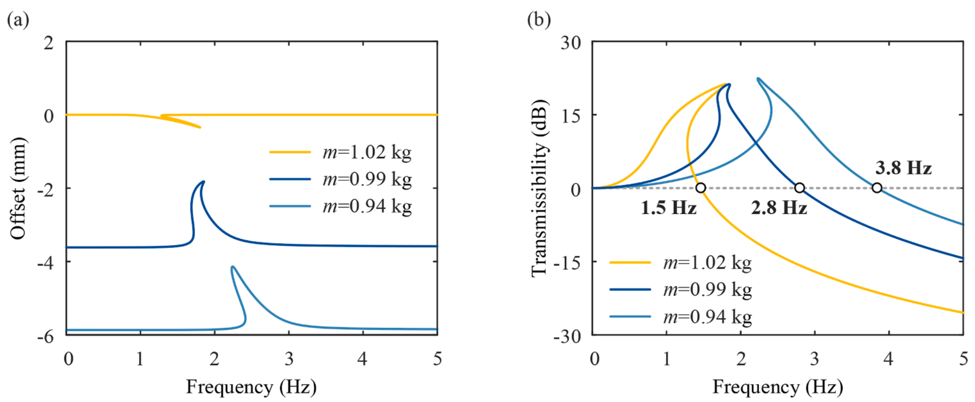

Fig. 18. Dynamic behavior under various load mismatches without rated load correction: (a) offset curves; (b) transmissibility curves.

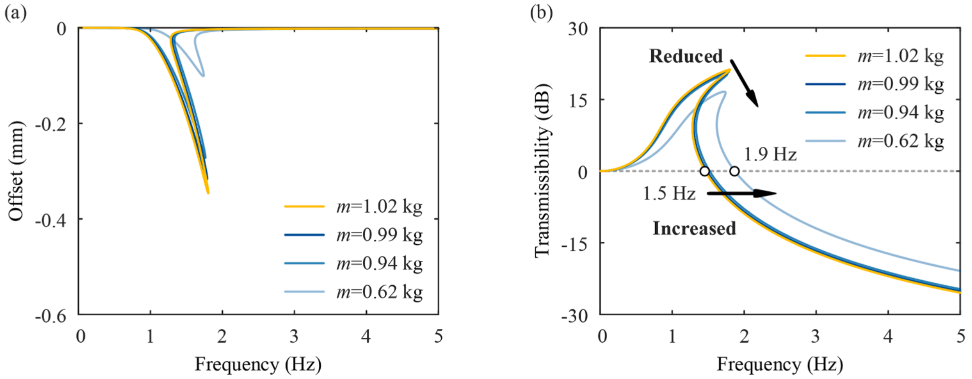

Fig. 19. Dynamic behavior under conventional rated load correction: (a) offset curves; (b) transmissibility curves.

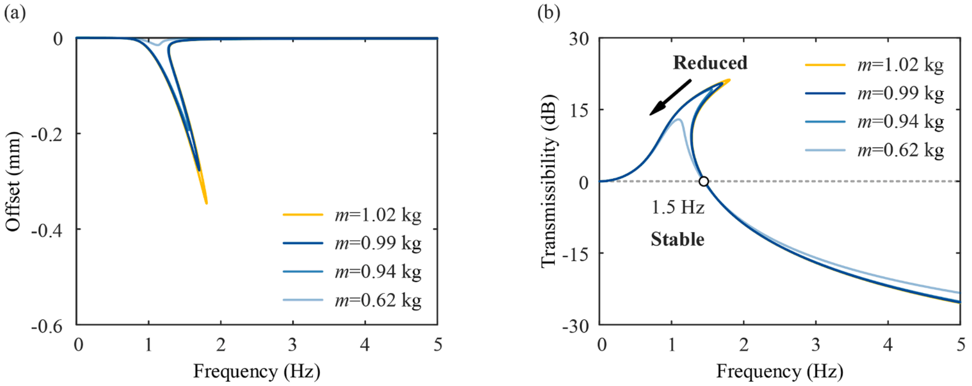

Fig. 20. Dynamic behavior under force-scaling rated load correction: (a) offset curves; (b) transmissibility curves.

performance. The larger the rated load of the RLC, the poorer the low-frequency vibration isolation becomes. For example, neglecting the jump phenomenon, when the applied load increases from $m = 0.62$ kg to $m = 1.02$ kg, the rated load of the RLC rises from 0.11 kg to 0.51 kg, and the starting isolation frequency increases from 1.67 Hz to 2.03 Hz. Fig. 21(b) presents the transmissibility curves under various imperfect conditions. As the natural frequency increases, the starting isolation frequency also rises, indicating a progressively deeper degradation in low-frequency vibration isolation performance. In addition, the increase in natural frequency reduces the damping coefficient, leading to a higher transmissibility peak. Conversely, as shown in Fig. 22, when $f_{re}<f_{pe}$, the decreased natural frequency of the RLC, resulting from weakened stiffness, shifts the resonance region toward lower frequencies. As the rated load of the RLC increases and its natural frequency decreases, the starting isolation frequency is further reduced, indicating unstable low-frequency vibration isolation performance. Therefore, mismatches in the natural frequencies between the RLC and the passive QZS isolator should be avoided to ensure stable low-frequency vibration isolation performance.

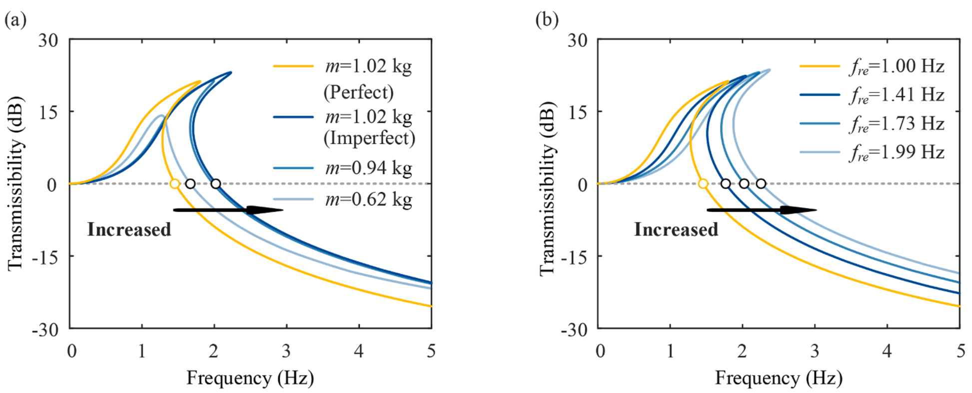

Fig. 21. Transmissibility curves under $f_{re}>f_{pe}$: (a) various rated loads; (b) various natural frequencies.

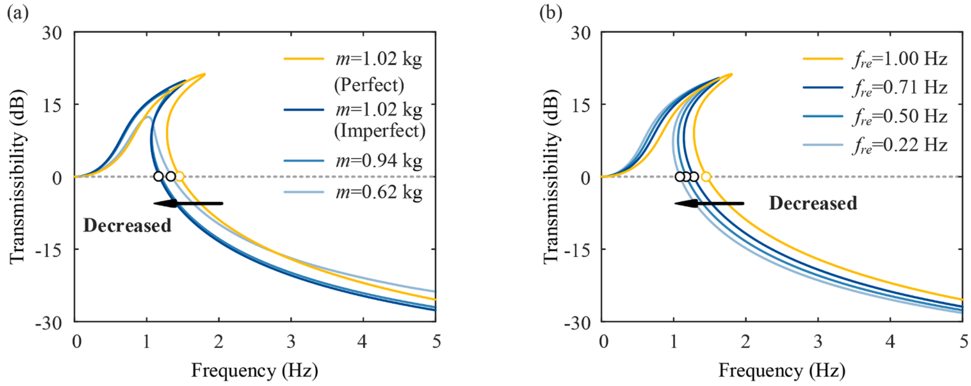

Fig. 22. Transmissibility curves under $f_{re}<f_{pe}$: (a) various rated loads; (b) various natural frequencies.

6. Experimental identification and verification

6.1. Force-displacement relationship identification

The passive QZS isolator is implemented using the CCBS developed in our previous work [53]. An experimental prototype of the CCBS was fabricated, and its force-displacement relationship was measured using a universal testing machine with a feed rate of 10 mm/min. Each quarter-arc-shaped beam was made of spring steel, with a radius of 40 mm, a width of 5 mm, and a thickness of 0.3 mm. The elastic diaphragm was manufactured from a 0.45 mm-thick titanium sheet via laser cutting. Based on the experimental data, the corresponding fitting coefficients were identified with a low root-mean-square error of 0.003 N. As shown in Fig. 23, the rated load of the experimental prototype is 3.24 kg, and the corresponding stiffness is 0.015 N/mm, demonstrating a near-zero-stiffness characteristic.

An experimental prototype of the RLC was also fabricated, in which the permanent magnet was made of NdFeB, and both the positive- and negative-stiffness coils were tightly wound with copper wire. As shown in Fig. 24(a), the force-displacement relationships of the nested coil-magnet, end-to-end coil-magnet, and RLC were measured using a universal testing machine. In the setup, the permanent magnet was mounted on the movable workbench of the testing machine and driven to compress against the coils. The negative-stiffness and positive-stiffness coils were independently powered by two constant current sources (UNI-T UTP1306S), with the current sequentially set to 0.5 A, 1.0 A, and 1.5 A. The detailed parameter configuration of the RLC is listed in Table 2. Fig. 24(b, c) present the experimental results of the nested and end-to-end coil-magnet, respectively. Using the experimental data, polynomial fitting was performed for each current condition, and the resulting fitting coefficients were averaged to determine the coefficients in Eq. (14). The fitting curves exhibit excellent agreement with the experimental data, with mean root-mean-square errors of 0.015 N and 0.029 N for the nested and end-to-end coil-magnet, respectively. This validates the linear dependence of the electromagnetic force on the current.

According to Eq. (19), to correct the rated load of the passive QZS isolator without changing the natural frequency, the current ratio of the RLC was determined as I_r=3.252. Fig. 24(d) presents the force-displacement curve of the RLC when I_{c1}=0.2 A and I_{c2}=0.65 A. The theoretical results obtained using Eq. (13) are also presented for comparison, where the parameters are set as z_{c1}=35 mm, z_{c2}=1 mm, N_{w1}=22, N_{w2}=34, N_{h1}= 24, N_{h2}=48, N_m=24, B_r=1.212 T It can be observed that the RLC distinctly exhibits a QZS characteristic, with the equilibrium position located at a displacement of 8.62 mm, corresponding to a rated load of 0.41 kg and an ultra-low stiffness of 0.002 N/mm. The natural frequencies of the RLC and the passive QZS are both close to 0.35 Hz. Moreover, the experimental results

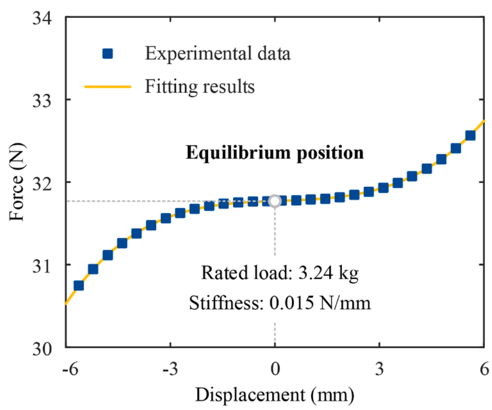

Fig. 23. Force-displacement relationship identification of the passive QZS isolator.

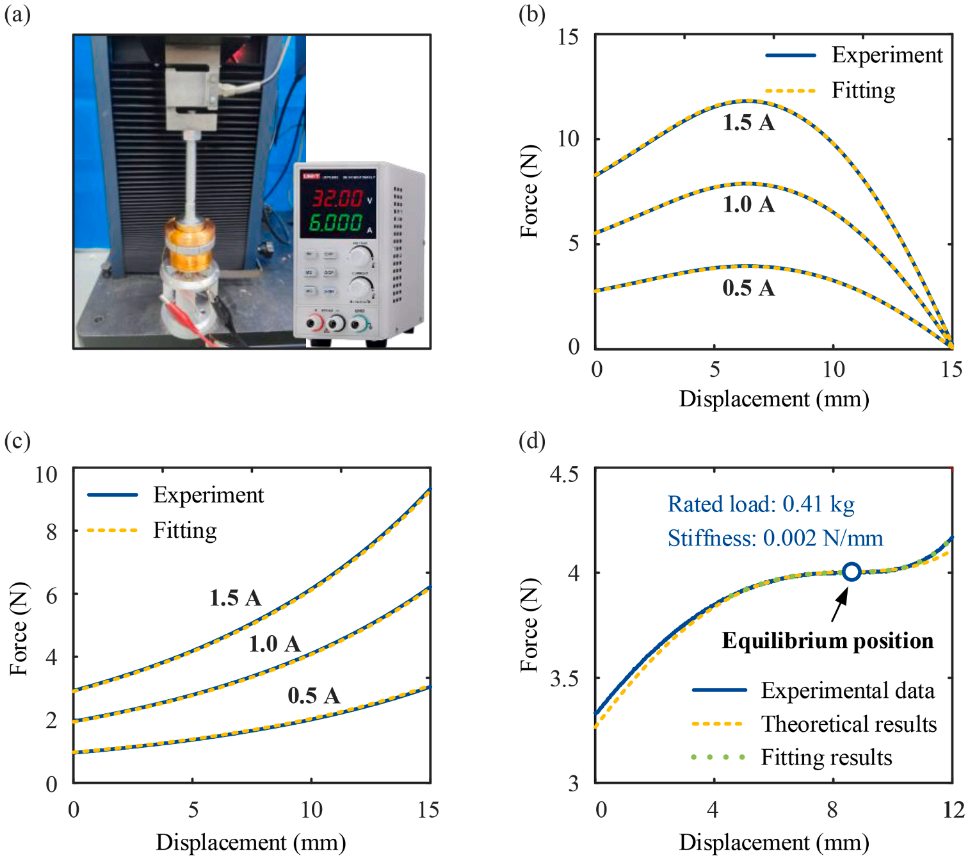

Fig. 24. Force-displacement relationship identification of the nested coil-magnet, end-to-end coil-magnet, and RLC: (a) experimental system; (b) nested coil-magnet; (c) end-to-end coil-magnet; (d) RLC.

show good agreement with the theoretical predictions, with the small discrepancies mainly attributed to manufacturing and assembly tolerances. Build on the experimental data, the corresponding coefficients in Eq. (22) were identified with I_{c10}=0.2 A and I_{c20}=0.65 A.

6.2. Offline rated load correction test

The offline rated load correction test was conducted to verify the effectiveness of the force-scaling rated load correction method in enabling stable low-frequency vibration isolation. The experimental setup for the tests is shown in Fig. 25, where the experimental prototype of the vibration isolator combining the RLC and passive QZS isolator is mounted on the workbench of an electromagnetic shaker (SINOCERA PIEZOTRONICS JZK-100). Through feedback control, the shaker can perform stable periodic, sweeping, and random motions according to preset excitation signals, enabling comprehensive base excitation testing of the QZS-RLC. For the periodic excitation test, a signal generator (Tektronix AFG3022C) is used to produce a predefined harmonic excitation signal, which is then amplified by a power amplifier (SINOCERA YE5878) to drive the shaker. Two laser displacement sensors (Panasonic HL-G103-A-C5, 0.5 μm resolution) are employed to measure the base excitation displacement and the load response displacement, respectively. The measurement data are acquired using a dynamic signal analyzer (DONDHUA DG5902) at a sampling frequency of 500 Hz and recorded on a computer. For the sweeping and random excitation tests, the predefined excitation signals are generated by the computer and used to control the shaker via a vibration controller (ECON VT-9008), which implements closed-loop control based on acceleration feedback. As in the periodic test, the excitation signals are amplified through the power amplifier before being used to drive the shaker and apply base excitation to the vibration isolator. Two accelerometers (HOUDE HD-YD-232, 112.41 mV/g sensitivity) are used to measure the base excitation and load response accelerations, respectively. The acceleration data are also collected by the dynamic signal analyzer and recorded by the computer. The negative-stiffness and positive-stiffness coils are energized by two constant current sources (UNI-T UTP1306S), respectively, as in the static test. The output current is regulated manually.

The periodic excitation test was first conducted to evaluate the vibration isolation performance of the passive QZS isolator. The excitation amplitude was set to 0.21 mm, and the frequency range spanned from 0.1 Hz to 2 Hz. The RLC was deactivated, and the passive QZS isolator was sequentially loaded with 3250 g, 3260 g, and 3270 g, with 3250 g defined as the rated load. Fig. 26(a-d) show the time histories of the base excitation and load response displacements at excitation frequencies of 0.3 Hz, 0.5 Hz, 1.0 Hz, and 2.0 Hz. When the applied load is set to the rated value, at 0.3 Hz and 0.5 Hz, the load response displacement exceeds the base excitation

Table 2
Parameter configuration of the RLC.

Parameters of the RLC	Value
Inner radii of the negative-stiffness and positive-stiffness coils, r_{c1}/r_{c2}	19 mm/9.5 mm
Widths of the negative-stiffness and positive-stiffness coils, w_{c1}/w_{c2}	11 mm/17.5 mm
Heights of the negative-stiffness and positive-stiffness coils, h_{c1}/h_{c2}	12 mm/25 mm
Inner radius, width, and height of the permanent magnet, $r_m/w_m/h_m$	5 mm/13 mm/12 mm
Gap between the negative-stiffness and positive-stiffness coils	9 mm
Copper wire diameter	0.5 mm

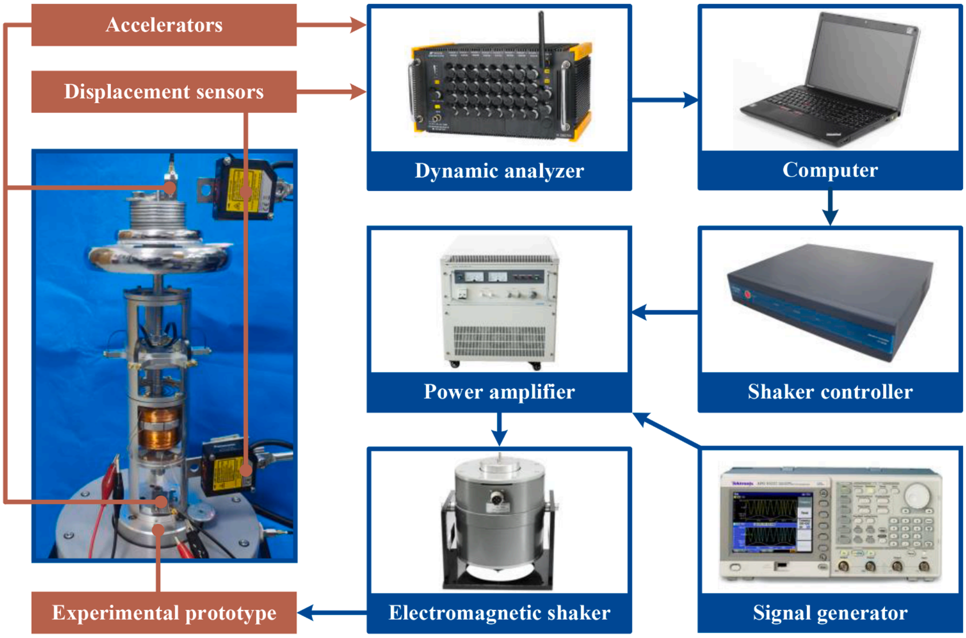

Fig. 25. Rated load correction test system.

displacement, indicating amplification of the input excitation. In contrast, at 1.0 Hz and 2.0 Hz, the load response displacement is smaller than the base excitation displacement, demonstrating effective vibration attenuation. The transmissibility curve plotted in Fig. 26(e) reveals a resonance peak at 0.5 Hz and shows that vibrations above 0.8 Hz are effectively suppressed, showing an ultra-low frequency vibration isolation performance. When the applied load is increased by merely 10 g (0.31% of the rated load), the vibration isolator enters a load-mismatched state, with the resonant frequency and starting isolation frequency shifting to 0.9 Hz and 1.4 Hz, respectively. A further 10 g increase in applied load caused the starting isolation frequency to deteriorate sharply to 2.0 Hz. The theoretical transmissibility curves at the rated load and with a 10 g load mismatch are plotted for comparison, with the damping selected to align the peak values of the theoretical and experimental curves under the 10 g load mismatch. It can be seen that the theoretical and experimental resonance frequencies and isolation starting frequencies differ by only about 0.1 Hz, validating the effectiveness of the dynamic model. The periodic excitation results indicate that, due to its ultra-low stiffness characteristics, the passive QZS isolator exhibits excellent sub-frequency vibration isolation performance. However, it is also highly sensitive to variations in load, and even slight load mismatches can significantly degrade its isolation effectiveness at low frequencies.

To evaluate the offline performance of the force-scaling rated load correction method, a sweeping excitation test was conducted. Three loading conditions were set, with applied loads of 3250 g, 3657 g, and 4062 g. For each case, the coil currents of the RLC were adjusted to ensure that the rated load matched the applied load. Under each loading condition, three sets of sweeping excitations were applied sequentially to the base of the QZS-RLC. The frequency ranges from 1.5 Hz to 10 Hz, with a sweep duration of 50 s. The peak-to-peak excitation amplitudes were set to 0.3 mm, 0.4 mm, and 0.5 mm, respectively. Fig. 27(a) exhibits the time histories of the base excitation and load response accelerations under the applied load of 3250 g. Fig. 27(b-d) present the transmissibility curves for the applied loads of 3250 g, 3657 g, and 4062 g, respectively. As shown in Fig. 27(b), with the applied load of 3250 g and the RLC deactivated, the transmissibility reaches −40 dB from 3.6 Hz, indicating broadband vibration attenuation. When the applied load increases by 12.5% to 3657 g, a mismatch occurs between the applied load and the rated load. To eliminate this mismatch, the coil currents were adjusted to I_{c1}=0.2 A and I_{c2}=0.65 A, achieving the alignment between the applied load and the rated value. As illustrated in Fig. 27(c), the transmissibility reaches −40 dB at 4.1 Hz, demonstrating that the RLC has little adverse effect on the QZS characteristics and that the broadband attenuation performance is maintained. Similarly, as shown in Fig. 27(d), when the applied load

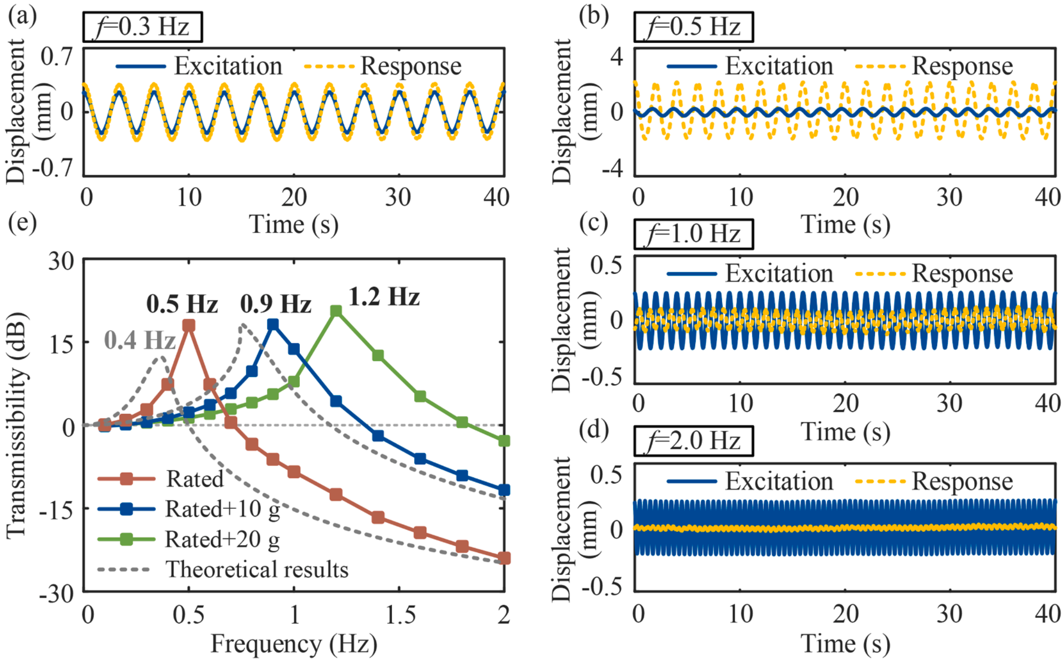

Fig. 26. Periodic excitation test results of the passive QZS isolator: (a)-(d) time histories of the excitation and response displacements at 0.3 Hz, 0.5 Hz, 1.0 Hz, and 2.0 Hz; (e) transmissibility.

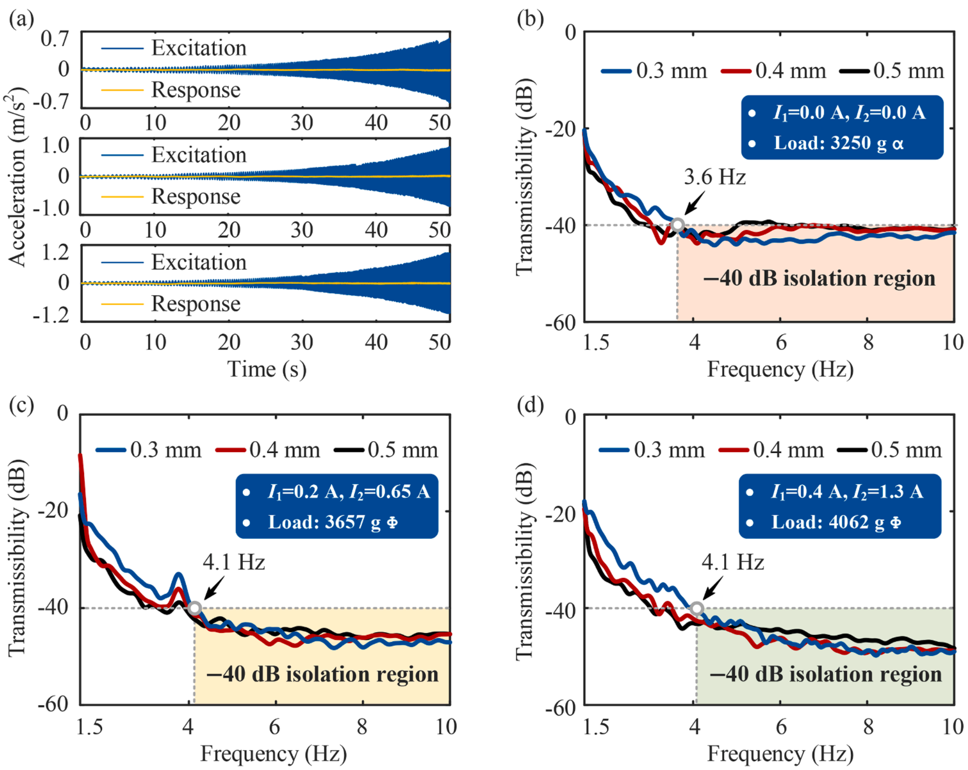

Fig. 27. Sweep excitation test results: (a) time histories of the excitation and response accelerations under the rated load; (b)-(d) transmissibility curves under applied loads of 3250 g, 3657 g, and 4062 g.

is increased by 25.0% to 4062 g and the coil currents are adjusted to I_{c1}=0.4 A and I_{c2}=1.3 A, the transmissibility still reaches −40 dB at 4.1 Hz. These results confirm the effectiveness of the force-scaling rated load correction method in achieving wide-range rated load correction and enhancing the reliability of low-frequency vibration isolation performance in passive QZS isolators.

In order to further validate the force-scaling rated load correction method, a random excitation test was conducted. During the test, the vibration isolator was sequentially loaded with 3250 g and 3657 g, and the rated load was matched to the applied load via rated load correction. The acceleration power spectral density of the random excitation was set to 0.0005 g^2/Hz within a frequency range of 5 Hz to 100 Hz. Fig. 28(a, b) show the time histories of the base excitation and load response accelerations under the applied loads of 3250 g and 3657 g, respectively. In both cases, the load response acceleration is significantly smaller than the base excitation acceleration. Fig. 28(c, d) summarize the maximum, mean, and root-mean-square (RMS) values of the base and response accelerations under the two loading conditions. As shown in Fig. 28(c), when the applied load is 3250 g and the RLC is deactivated, the maximum, mean, and RMS values of the base excitation acceleration are 9.50 m/s^2, 1.83 m/s^2, and 2.30 m/s^2, respectively, while those of the load response acceleration are 0.127 m/s^2, 0.024 m/s^2, and 0.030 m/s^2. Under the action of the vibration isolator, the maximum, mean, and RMS accelerations are reduced by 98.6%, 98.7%, and 98.7%, respectively. These results further verify the broadband vibration suppression capability of the passive QZS isolator, achieving an average vibration attenuation exceeding 98.5%. When the applied load increases to 3657 g, the coil currents are adjusted to I_{c1}=0.2 A and I_{c2}=0.65 A to match the increased applied load. As shown in Fig. 28 (d), the maximum, mean, and RMS values of the load response acceleration are 0.335 m/s^2, 0.045 m/s^2, and 0.057 m/s^2, corresponding to reductions of 96.5%, 97.6%, and 97.5%, respectively. These results indicate that the force-scaling rated load correction successfully compensates for variations in the applied load, preventing performance degradation caused by load mismatch.

6.3. Online rated load correction test

For a more comprehensive evaluation of the force-scaling rated load correction method during the operation of the vibration isolator, an online test was conducted. The experimental setup was identical to that of the offline rated load correction. The excitation amplitude was set to 0.21 mm, with excitation frequencies sequentially set to 0.4 Hz, 0.5 Hz, 0.6 Hz, 0.8 Hz, 0.9 Hz, and 1.0 Hz. At the beginning of the test, the initial applied load of the vibration isolator was 3250 g, and the RLC was turned off, ensuring that the applied load matched the rated load. Subsequently, a 10 g mismatch load was applied to the QZS-RLC. After system stabilization, the RLC was activated to re-establish the match between the rated load and the applied load.

Fig. 29(a) shows the time histories of the base excitation and load response displacements at the excitation frequency of 0.9 Hz. At the initial test stage, since the starting isolation frequency is 0.8 Hz under the applied load of 3250 g, the 0.9 Hz excitation is effectively

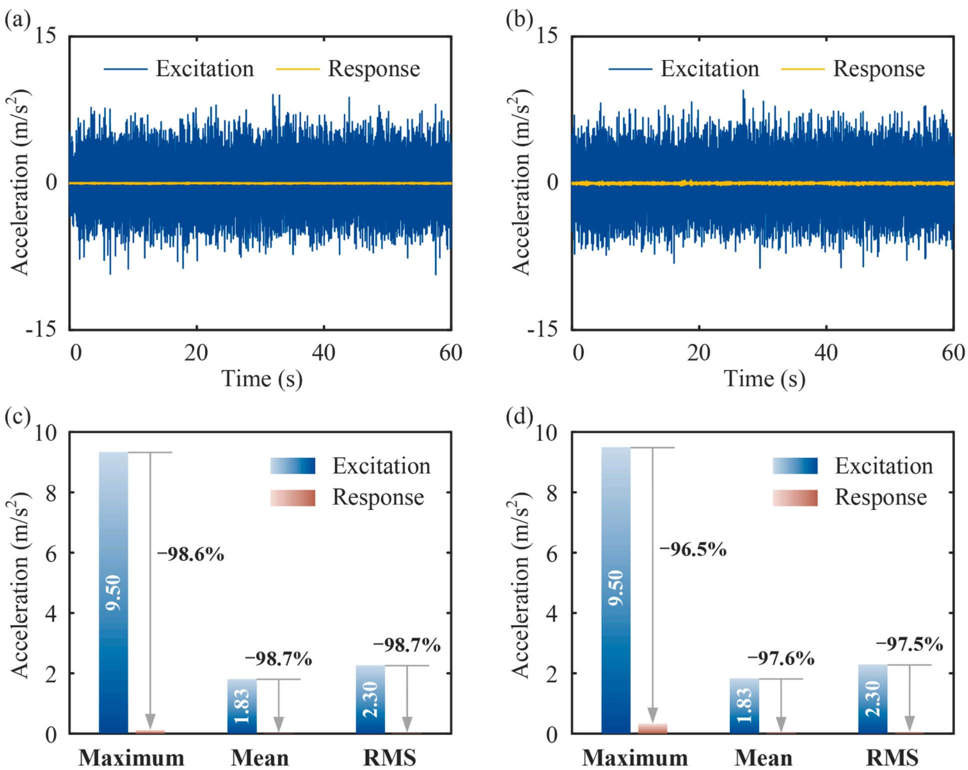

Fig. 28. Random excitation test results: (a)-(b) time histories of the excitation and response accelerations under applied loads of 3250 g and 3657 g; (c)-(d) maximum, mean, and RMS values of the excitation and response accelerations under applied loads of 3250 g and 3657 g.

attenuated. This results in the load response displacement being smaller than the base excitation displacement. When a 10 g mismatch load is applied, the rated load becomes lower than the applied load, causing a deviation from the equilibrium position and an increase in stiffness. As a result, the load response displacement rises significantly, exceeding the base excitation. It is worth noting that when the RLC is activated, the rated load realigns with the applied load and the ultra-low stiffness characteristic is restored, thereby reducing the load response displacement and recovering the ultra-low frequency vibration isolation performance. More importantly, the equilibrium position hardly changes, confirming the *in-situ* rated load correction capability of the force-scaling rated load correction method. Fig. 29(b) presents the time histories of the base excitation and load response displacements under the excitation frequency of 0.5 Hz. When the applied load is 3250 g, as this excitation frequency corresponds to the resonant frequency of the CCBS, the initial load response displacement is significantly larger than the base excitation displacement. After applying the 10 g mismatch load, the change in stiffness shifts the resonant frequency so that the amplification at 0.5 Hz disappears. When the RLC is subsequently activated, the ultra-low stiffness characteristic is recovered, and the resonant frequency returns to 0.5 Hz, leading to strong amplification of the base excitation once again. Fig. 29(c-f) show the time histories of the base and load response displacements at excitation frequencies of 0.4 Hz, 0.6 Hz, 0.8 Hz, and 1.0 Hz. The trends observed are similar to those under 0.9 Hz and 0.5 Hz excitations, and are therefore not elaborated repeatedly.

A Fast Fourier Transform was performed on the base excitation and the steady-state load response displacements at three stages: the initial test stage, after applying the mismatch load, and after activating the RLC. The displacement transmissibility at each stage was then calculated. As shown in Fig. 29(g), during the initial test stage, the applied load is equal to the rated load. At this point, the vibration isolator exhibits ultra-low stiffness characteristics, with a resonant frequency of 0.5 Hz and a starting isolation frequency of

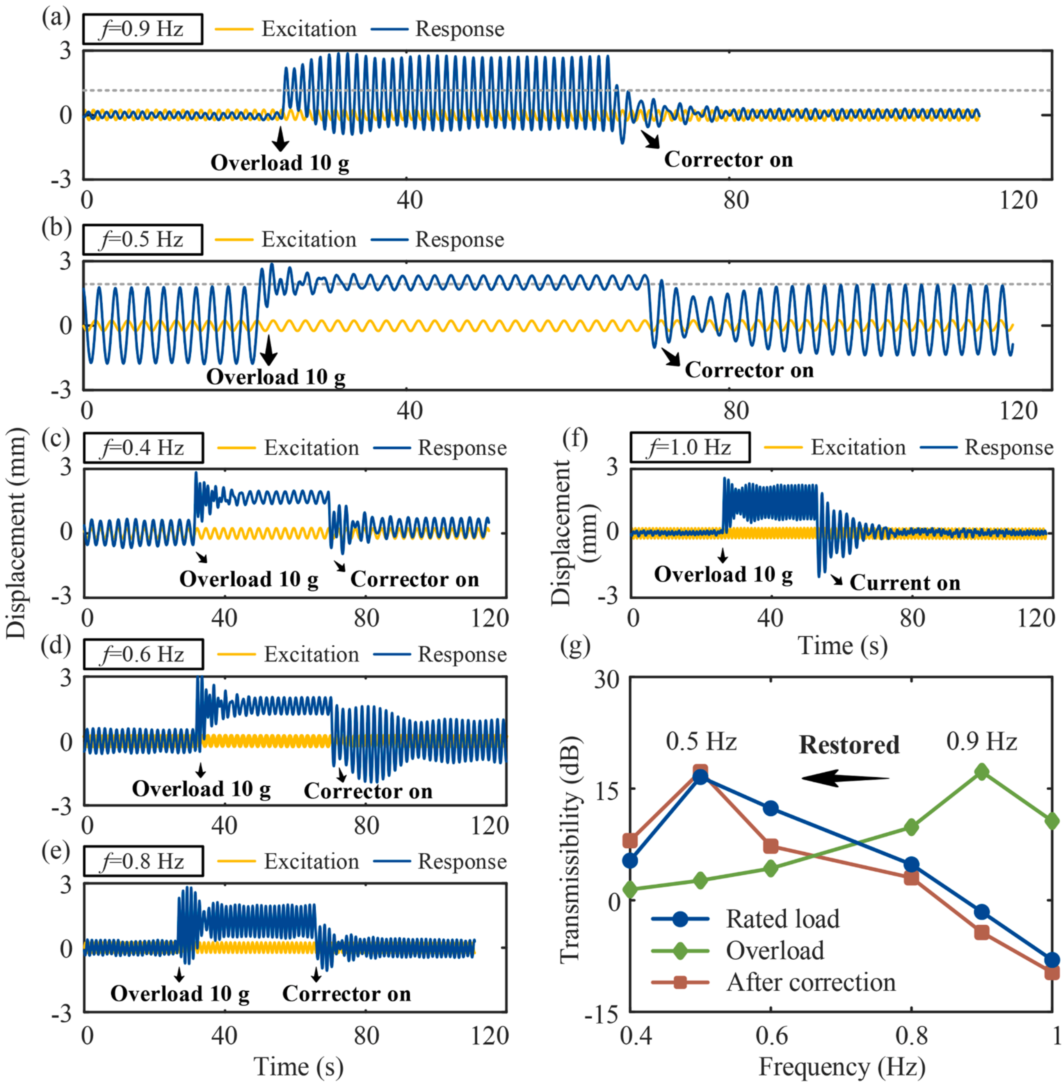

Fig. 29. Online rated load correction test results: (a)-(f) time histories of the excitation and response displacements at 0.9 Hz, 0.5 Hz, 0.4 Hz, 0.6 Hz, 0.8 Hz, and 1.0 Hz; (g) transmissibility before and after correction.

0.9 Hz, demonstrating ultra-low frequency vibration isolation performance. When a 10 g mismatch load is applied, the operating position of the vibration isolator deviates from the equilibrium position, increasing the stiffness and shifting the resonant frequency upward to 0.9 Hz, leading to the degradation of ultra-low frequency vibration isolation performance. However, after the RLC is activated and the rated load is realigned with the applied load, the vibration isolator regains its ultra-low stiffness characteristic. Consequently, the resonant frequency and the starting isolation frequency dropped back to 0.5 Hz and 0.9 Hz, respectively, and ultra-low frequency vibration isolation performance is restored. These results validate that the force-scaling rated correction enables real-time and fine-tuned adjustment of the rated load and can rapidly restore degraded vibration isolation performance caused by variations in the applied load during operation. This significantly improves the reliability of low-frequency vibration isolation under time-varying load conditions.

7. Conclusion

To address the issue of high sensitivity of low-frequency vibration isolation performance to load mismatch in QZS isolator design, this paper proposes a novel force-scaling rated load correction method. Unlike conventional load compensation and rated load adjustment methods, which inevitably alter the natural frequency during load mismatch elimination, the proposed method, as a control-free QZS isolator, achieves rated load correction through scaling of the force-displacement curve of an RLC. As a result, *in-situ* and continuous rated load correction can be realized without modifying the original natural frequency, thereby maintaining stable low-frequency vibration isolation performance over a wide range of load variations. To validate the proposed concept, an RLC based on electromagnetic force scaling is developed and integrated into a passive QZS isolator. Both theoretical and experimental investigations demonstrate that the electromagnetic force can be continuously regulated through the coil current, providing the required force-scaling capability for rated load correction. Static and dynamic comparisons with conventional methods further confirm that the proposed approach effectively eliminates load mismatch while preserving a constant natural frequency, resulting in significantly more stable vibration isolation performance. Moreover, periodic, swept-frequency, and random excitation experiments verify the effectiveness of the method in both offline and online rated load correction under various operating conditions. The proposed force-scaling-based rated load correction method offers a new paradigm for improving the robustness of QZS isolators against load mismatch. By maintaining quasi-constant natural frequency throughout the load correction process, it provides a practical, reliable, and energy-efficient solution for achieving stable ultra-low-frequency vibration isolation under wide-range and time-varying loading conditions. Future work might focus on extending the force-scaling concept to multi-degree-of-freedom QZS systems and developing adaptive load correction strategies for more complex operating environments.

CRediT authorship contribution statement

Jia-Jia Lu: Writing – original draft, Visualization, Validation, Methodology, Investigation, Formal analysis, Data curation, Conceptualization. **Tian-Yu Zhao:** Visualization, Validation, Software, Formal analysis. **Fan-Chi Zeng:** Visualization, Validation, Software. **Wen-Hao Qi:** Validation. **Ge Yan:** Writing – review & editing, Visualization, Funding acquisition. **Li Cheng:** Writing – review & editing, Supervision. **Wen-Ming Zhang:** Writing – review & editing, Supervision, Project administration, Conceptualization.

Declaration of competing interest

The authors declare that they have no known competing financial interests or personal relationships that could have appeared to influence the work reported in this paper.

Acknowledgement

The authors gratefully acknowledge the support by the Fundamental and Interdisciplinary Disciplines Breakthrough Plan of the Ministry of Education of China (Grant No. JYB2025XDXM214), Fundamental Research Funds for the Central Universities, Leading Scientific Research Project of China National Nuclear Corporation, National Natural Science Foundation of China (Grant Nos. 12121002, 12032015, 12302020), Scientific and Innovative Action Plan of Shanghai (Grant No. 21190760100), and Postdoctoral Fellowship Program of CPSF (Grant No. GZB20230410).

Supplementary materials

Supplementary material associated with this article can be found, in the online version, at doi:10.1016/j.jsv.2026.120066.

Data availability

No data was used for the research described in the article.

References

[1] Y. Yang, H.L. Liu, J.W. Yuan, W.L. Kong, M. Wan, W.H. Zhang, Development of an anti-vibration cutting tool combining the lattice structures infill with damping particles, Mech. Syst. Signal Process. 228 (2025) 112425.
[2] R. Lin, Y. Li, J. Qian, P. Cheng, X. Gao, W. Sun, Y. Hu, Q. Yuan, Design of a vibration isolation platform for atomic force microscope based on flexural structure, Precis. Eng. 89 (2024) 113–120.
[3] Z.B. Li, L. Li, J.Q. Zhang, W.C. Feng, System modeling and sliding mode control of fast steering mirror for space laser communication, Mech. Syst. Signal Process. 211 (2024) 111206.
[4] Y. Du, Z. Liang, Z. Gao, S. Chen, Y. Yue, J. Zhang, H. Liu, H. Zheng, B. Liu, T. Qiu, Z. Liu, Investigation on the dominant mechanism of chatter in high-load robot milling process based on theoretical and experimental analysis, J. Sound Vib. 600 (2025) 118886.
[5] K. Nasiri, H. Moradi, Chatter suppression in nonlinear milling of a flexible plate-workpiece with attached piezoelectric actuators: comparison of soft-actor-critic-based controller vs optimized type-2 fuzzy controller, Mech. Syst. Signal Process. 224 (2025) 112198.
[6] D.L. Zou, L. Xue, Q. Lin, J.H. Xu, X.G. Dong, N. Ta, Z.S. Rao, Influence of propulsion shafting longitudinal vibration on the excitation force and vortex dynamics characteristics of pump-jet propulsor, Ocean Eng. 295 (2024) 116962.
[7] X. Ma, R. Yu, H. Li, J. Jing, Z. Zhang, Vibration mitigation in a spline-shafting system via an auxiliary support: simulation and experiment, Mech. Syst. Signal Process. 224 (2025) 112120.
[8] M.U. Demir, C. Yilmaz, Realization of a wideband three-axis horizontal vibration isolator with adjustable stiffness and damping, J. Sound Vib. 600 (2025) 118876.
[9] T. Yang, Y.Q. Zhang, S.X. Zhou, Multistage oscillators for ultra-low frequency vibration isolation and energy harvesting, Sci. China-Technol. Sci. 65 (2022) 631–645.
[10] N. Yu, K. Yang, Z.M. Wu, W.M. Zhang, B. Yan, Low-frequency vibration absorption of magnetic quasi-zero-stiffness structures with lever mechanism, Int. J. Mech. Sci. 267 (2024) 108973.
[11] M. Umair, Z.C. Hou, A novel high-static-low-dynamic-stiffness isolator with sliding mass: modeling and analysis, Nonlinear Dyn. 112 (2024) 9767–9781.
[12] K. Kocak, C. Yilmaz, Design of a compliant lever-type passive vibration isolator with quasi-zero-stiffness mechanism, J. Sound Vib. 558 (2023) 117758.
[13] W. Zhang, W.Q. Cheng, W. You, X. Chen, J. Zhang, C. Li, C. Fang, Levitated-body ultra-high pointing accuracy and stability satellite platform of the CHASE mission, Sci. China-Phys. Mech. Astron. 65 (2022) 289604.
[14] Y.T. Zhang, G.N. Zhu, Q.J. Cao, Isolation performances and optimization of triple quasi-zero stiffness isolators, Sci. China-Phys. Mech. Astron. 67 (2024) 274511.
[15] A. Carrella, M.J. Brennan, I. Kovacic, T.P. Waters, On the force transmissibility of a vibration isolator with quasi-zero-stiffness, J. Sound Vib. 322 (2009) 707–717.
[16] A. Carrella, M.J. Brennan, T.P. Waters, Static analysis of a passive vibration isolator with quasi-zero-stiffness characteristic, J. Sound Vib. 301 (2007) 678–689.
[17] A. Carrella, M.J. Brennan, T.P. Waters, V. Lopes, Force and displacement transmissibility of a nonlinear isolator with high-static-low-dynamic-stiffness, Int. J. Mech. Sci. 55 (2012) 22–29.
[18] G. Gatti, A.D. Shaw, P.J.P. Goncalves, M.J. Brennan, On the detailed design of a quasi-zero stiffness device to assist in the realisation of a translational Lanchester damper, Mech. Syst. Signal Process. 164 (2022) 108258.
[19] F. Eskandary-Malayery, S. Ilanko, B. Mace, Y. Mochida, F. Pellicano, Experimental and numerical investigation of a vertical vibration isolator for seismic applications, Nonlinear Dyn. 109 (2022) 303–322.
[20] Y. Shi, S.F. Xu, Z.L. Li, Y.X. Wang, Y.L. Nie, Z.B. Sun, Dynamic frequency response characteristics of a compound regulative quasi-zero stiffness air spring system, Sci. China-Technol. Sci. 66 (2023) 2013–2024.
[21] N.A. Saeed, L. Hou, H. Yi, A.A. Shukur, S.M. Alamry, S.M. El-Shourbagy, On a broadband vibration isolator with tunable stiffness: from quasi-zero-stiffness to zero-stiffness behavior, Appl. Mathe. Mech. 47 (2026) 255–282.
[22] X.C. Huang, X.T. Liu, J.Y. Sun, Z.Y. Zhang, H.X. Hua, Vibration isolation characteristics of a nonlinear isolator using Euler buckled beam as negative stiffness corrector: a theoretical and experimental study, J. Sound Vib. 333 (2014) 1132–1148.
[23] M.Q. Niu, Y.S. Zhuang, W.J. Han, L.Q. Chen, History dependent analysis of compliant beams for nonlinear vibration isolation, Int. J. Mech. Sci. 281 (2024) 109571.
[24] G.D. Sui, C.Y. Zhou, Y.F. Chen, X.F. Zhang, C.W. Hou, X.B. Shan, J. Cao, Research on flexible beam-type nonlinear vibration isolators suitable for low frequencies, Ocean Eng. 293 (2024) 116652.
[25] B.X. Ding, X. Li, S.C. Chen, Y.M. Li, Modular quasi-zero-stiffness isolator based on compliant constant-force mechanisms for low-frequency vibration isolation, J. Vib. Control 30 (2024) 3006–3020.
[26] J.X. Zhou, X.L. Wang, D.L. Xu, S. Bishop, Nonlinear dynamic characteristics of a quasi-zero stiffness vibration isolator with cam-roller-spring mechanisms, J. Sound Vib. 346 (2015) 53–69.
[27] J.X. Zhou, Q.Y. Xiao, D.L. Xu, H.J. Ouyang, Y.L. Li, A novel quasi-zero-stiffness strut and its applications in six-degree-of-freedom vibration isolation platform, J. Sound Vib. 394 (2017) 59–74.
[28] K. Wang, J.X. Zhou, D.L. Xu, Sensitivity analysis of parametric errors on the performance of a torsion quasi-zero-stiffness vibration isolator, Int. J. Mech. Sci. 134 (2017) 336–346.
[29] M. Wang, S.B. Fu, J.H. Ding, Y. Sun, Y. Peng, J. Luo, H.Y. Pu, Analytical and experimental validation of vibration isolation system with complementary stiffness and composite control, Aerosp. Sci. Technol. 133 (2023) 108117.
[30] S.J. Yuan, A.P. Sun, Q.M. Li, J.H. Zhu, L. Hou, J.L. Zhao, J. Yi, H.Y. Pu, J. Luo, Semi-active control of the electromagnetic negative stiffness mechanism in a double-layer vibration isolator, Nonlinear Dyn. 112 (2024) 13951–13969.
[31] J.-J. Lu, G. Yan, Y.-B. Cao, W.-H. Qi, F.-R. Liu, W.-M. Zhang, Integration of nonlinear-vibration-isolation and actuation: design and control, IEEE/ASME Trans. Mechatron. 30 (2025) 7137–7148.
[32] Q. Wang, J.X. Zhou, K. Wang, D.L. Xu, G.L. Wen, Design and experimental study of a compact quasi-zero-stiffness isolator using wave springs, Sci. China-Technol. Sci. 64 (2021) 2255–2271.
[33] Z.H. Zhu, Y. Wang, Y. Wang, X.J. Jing, Nonlinear inertia and its effect within an X-shaped mechanism-part I: modelling & nonlinear properties, Mech. Syst. Signal Process. 200 (2023) 110590.
[34] X.J. Jing, The X-structure/mechanism approach to beneficial nonlinear design in engineering, Appl. Math. Mech.-Engl. Ed. 43 (2022) 979–1000.
[35] X.T. Sun, X.J. Jing, Analysis and design of a nonlinear stiffness and damping system with a scissor-like structure, Mech. Syst. Signal Process. 66-67 (2016) 723–742.
[36] X.J. Jing, Z.H. Zhu, Y.Q. Guo, S.H. Liu, Nonlinear inertia and its effect within an X-shaped mechanism-part II: nonlinear influences and experimental validations, Mech. Syst. Signal Process. 200 (2023) 110591.
[37] G. Yan, W.H. Qi, J.J. Lu, F.R. Liu, H. Yan, L.C. Zhao, Z.Y. Wu, W.M. Zhang, Bio-inspired multi-joint-collaborative vibration isolation, J. Sound Vib. 568 (2024) 118089.
[38] G. Yan, H.X. Zou, S. Wang, L.C. Zhao, Z.Y. Wu, W.M. Zhang, Bio-inspired vibration isolation: methodology and design, Appl. Mech. Rev. 73 (2021) 020801.
[39] X.T. Sun, Z.F. Qi, J. Xu, Vibration properties of a knee bio-inspired nonlinear isolation structure, Int. J. Non-Linear Mech. 147 (2022) 104245.
[40] B. Yan, P. Ling, L.L. Miao, N. Yu, J.J. Sun, Q.C. Li, Ultra-low vibration isolation of cockroach-inspired structures with electromagnetic shunt damping enhanced by geometric nonlinearity, IEEE-ASME Trans. Mechatron. 29 (2024) 476–486.
[41] J.C. Ji, Q.T. Luo, K. Ye, Vibration control based metamaterials and origami structures: a state-of-the-art review, Mech. Syst. Signal Process. 161 (2021) 107945.
[42] K. Ye, J.C. Ji, R. Fitch, Further investigation and experimental study of an origami structure-based quasi-zero-stiffness vibration isolator, Int. J. Non-Linear Mech. 157 (2023) 104554.

[43] X.T. Sun, Q. Lv, J.W. Qian, J. Xu, Vibration isolation platform for large-amplitude-low-frequency excitation by parallel-stack-assembly design of Miura origamis, Int. J. Non-Linear Mech. 166 (2024) 104831.
[44] K.F. Yu, Y.W. Chen, C.Y. Yu, J.R. Zhang, X. Lu, An origami-inspired low-frequency isolator with one/two-stage quasi-zero stiffness characteristics, Int. J. Mech. Sci. 289 (2025) 110040.
[45] K. Wang, J.X. Zhou, H. Ouyang, L. Cheng, D.L. Xu, A semi-active metamaterial beam with electromagnetic quasi-zero-stiffness resonators for ultralow-frequency band gap tuning, Int. J. Mech. Sci. 176 (2020) 105548.
[46] C.Q. Cai, J.X. Zhou, K. Wang, H.B. Pan, D.G. Tan, D.L. Xu, G.L. Wen, J.E. Mottershead, Flexural wave attenuation by metamaterial beam with compliant quasi-zero-stiffness resonators, Mech. Syst. Signal Process. 174 (2022) 109119.
[47] J.H. Zhong, J. Li, B.X. Ding, S.C. Chen, Design and experimental verification of programmable metastructures based on constant force cells, Smart Mater. Struct. 34 (2025) 015002.
[48] G. Yan, J.J. Lu, W.H. Qi, F.R. Liu, H. Yan, L.C. Zhao, Z.Y. Wu, W.M. Zhang, Linear and nonlinear stiffness compensation for low-frequency vibration isolation: a comparative study, Nonlinear Dyn. 112 (2024) 5955–5973.
[49] G. Yan, Z.Y. Wu, X.S. Wei, S. Wang, H.X. Zou, L.C. Zhao, W.H. Qi, W.M. Zhang, Nonlinear compensation method for quasi-zero stiffness vibration isolation, J. Sound Vib. 523 (2022) 116743.
[50] W.H. Qi, G. Yan, J.J. Lu, H. Yan, J.W. Shi, X.S. Wei, S. Wang, W.M. Zhang, Magnetically modulated sliding structure for low frequency vibration isolation, J. Sound Vib. 526 (2022) 116819.
[51] G. Yan, W.H. Qi, J.W. Shi, H. Yan, H.X. Zou, L.C. Zhao, Z.Y. Wu, X.Y. Fang, X.Y. Li, W.M. Zhang, Bionic paw-inspired structure for vibration isolation with novel nonlinear compensation mechanism, J. Sound Vib. 525 (2022) 116799.
[52] T.Y. Zhao, G. Yan, W.H. Qi, J.J. Lu, W.M. Zhang, Magnetically modulated tetrahedral structure for low frequency vibration isolation with adjustable load capacity, Int. J. Mech. Sci. 251 (2023) 108335.
[53] J.J. Lu, W.H. Qi, F.R. Liu, Y.B. Cao, T.Y. Zhao, L.Q. Cai, Y. Li, G. Yan, W.M. Zhang, Compliant curved beam support with flexible stiffness modulation for near-zero frequency vibration isolation, J. Sound Vib. 595 (2025) 118702.
[54] Q.Y. Meng, L. Hou, A.W. Wang, R.Z. Lin, Z.G. Li, S. Zhong, Y.S. Chen, N.A. Saeed, A.F. Mohamed, E.M. Awwad, Subharmonic response suppression of a quasi-zero stiffness system, J. Sound Vib. (2025) 594.
[55] N.A. Saeed, L. Hou, G.M. Moatimid, S. Zhong, F.Z. Duraihem, Nonlinear dynamics of a bio-inspired 2-DOF low-frequency X-shaped vibration isolator with m-to-n layers driven harmonically under simultaneous primary and 1:1 internal resonances, Chaos Solit. Fract. (2025) 190.
[56] I. Kovacic, M.J. Brennan, B. Lineton, Effect of a static force on the dynamic behaviour of a harmonically excited quasi-zero stiffness system, J. Sound Vib. 325 (2009) 870–883.
[57] A. Abolfathi, M.J. Brennan, T.P. Waters, B. Tang, On the effects of mistuning a force-excited system containing a quasi-zero-stiffness vibration isolator, J. Vib. Acoust.-Trans. ASME 137 (2015) 044502.
[58] J.H. An, G.P. Chen, X. Deng, C. Xi, T. Wang, H. He, Analytical study of a pneumatic quasi-zero-stiffness isolator with mistuned mass, Nonlinear Dyn. 108 (2022) 3297–3312.
[59] W.-H. Qi, G. Yan, J.-J. Lu, F.-R. Liu, T.-Y. Zhao, H. Yan, W.-M. Zhang, Local gravity control method for solving load-mismatch issue in isolators, Int. J. Mech. Sci. 265 (2024) 108891.
[60] K. Sun, J. Tang, Y. Yang, B. Jiang, Y. Li, D. Cao, Active control of quasi-zero-stiffness vibration isolator with variable load, Int. J. Struct. Stab. Dyn. 24 (2024) 2450243.
[61] A.D. Shaw, G. Gatti, P.J.P. Gonçalves, B. Tang, M.J. Brennan, Frictional phenomena within a quasi zero stiffness vibration device, Mech. Syst. Signal Process. 211 (2024) 111113.
[62] S. Solaiachari, J. Lakshmipathy, Vibration control of an unbalanced system using a quasi-zero stiffness vibration isolator with fluidic actuators and composite material: an experimental study, J. Vib. Control 29 (2023) 689–699.
[63] R. Zhou, Y.F. Zhou, X.D. Chen, W.J. Hou, C. Wang, H. Wang, W. Jiang, Gravity compensation method via magnetic quasi-zero stiffness combined with a quasi-zero deformation control strategy, Sci. China-Technol. Sci. 65 (2022) 1738–1748.
[64] C.C. Lan, S.A. Yang, Y.S. Wu, Design and experiment of a compact quasi-zero-stiffness isolator capable of a wide range of loads, J. Sound Vib. 333 (2014) 4843–4858.
[65] Y. Chang, Y. Li, J. Zhou, K. Wang, Q. Wang, G. Wen, Compensation strategy for quasi-zero-stiffness vibration isolator under payload mismatch, Acta Mech. Sin. 40 (2024) 524033.
[66] Y. Zheng, W.-B. Shangguan, Z. Yin, X.-A. Liu, Design and modeling of a quasi-zero stiffness isolator for different loads, Mech. Syst. Signal Process. 188 (2023) 110017.
[67] Y.L. Li, Z.Y. Wu, Y. Peng, S. Yao, J.X. Zhou, Full-band vibration isolation of multi-step quasi-zero stiffness systems, Int. J. Mech. Sci. 274 (2024) 109277.
[68] K. Ye, J.C. Ji, T. Brown, Design of a quasi-zero stiffness isolation system for supporting different loads, J. Sound Vib. 471 (2020) 115198.
[69] Q.Y. Meng, L. Hou, R.Z. Lin, Y.S. Chen, N.A. Saeed, A. Fouly, E.M. Awwad, On a quasi-zero stiffness vibration isolator with multiple zero stiffness points for mass load deviation, Appl. Math. Model. (2025) 145.
[70] Q. Zhang, D.K. Guo, G.K. Hu, Tailored mechanical metamaterials with programmable quasi-zero-stiffness features for full-band vibration isolation, Adv. Funct. Mater. 31 (2021) 2101428.
[71] M. Zhang, X. Jing, A bioinspired dynamics-based adaptive fuzzy SMC method for half-car active suspension systems with input dead zones and saturations, IEEE T. Cybern. 51 (2021) 1743–1755.
[72] M.H. Zhang, X.J. Jing, W.J. Huang, P.R. Li, Saturated PD-SMC method for suspension systems by exploiting beneficial nonlinearities for improved vibration reduction and energy-saving performance, Mech. Syst. Signal Process. 179 (2022) 109376.
[73] N.Y.P. Vo, T.D. Le, Adaptive pneumatic vibration isolation platform, Mech. Syst. Signal Process. 133 (2019) 106258.
[74] J.J. Lu, G. Yan, W.H. Qi, H. Yan, J.W. Shi, A. Chen, W.M. Zhang, Load-adaptive quasi-zero stiffness vibration isolation via dual electromagnetic stiffness regulation, J. Sound Vib. 567 (2023) 118059.